이학박사 학위논문

Development of an Antiviral Drug Screening Platform and a Bioactive Implant Material by Using Graphene Oxide

산화그래핀을 이용한 항바이러스 약물 스크리닝 플랫폼 및 생리활성 임플란트 소재 개발

2022 년 2 월

서울대학교 대학원

화학부 나노바이오화학 전공

김 정 호

Ph. D. DISSERTATION

Development of an Antiviral Drug Screening Platform and a Bioactive Implant Material by Using Graphene Oxide

by

Jungho Kim

Supervisor: Prof. Dal-Hee Min

February, 2022

Department of Chemistry

Graduate School

Seoul National University

Development of an Antiviral Drug Screening Platform and a Bioactive Implant Material by Using Graphene Oxide

지도교수 민 달 희

이 논문을 이학박사학위논문으로 제출함

2021 년 12 월

서울대학교 대학원

화학부 나노바이오화학 전공

김 정 호

김 정 호 의 박사학위논문을 인준함

2021 년 12 월

위 원 장	홍 종 인	(인)
부위원장	민 달 희	(인)
위 원	홍 병 희	(인)
위 원	이 연	(인)
위 원	장 홍 제	(인)

Abstract

Development of an Antiviral Drug Screening Platform and a Bioactive Implant Material by Using Graphene Oxide

Jungho Kim
Department of Chemistry
The Graduate School
Seoul National University

Novel technologies to treat diseases, such as tissue engineering and drug discovery methodologies, have developed in conjunction with advances in civilization and science. However, certain problems in the field of life sciences have not received sufficient attention and remain unresolved. A classic example is the discovery of therapeutic agents for viral infections. In the globalized modern society, it is imperative to protect and treat humanity from viral infections. However, due to the diversity of viruses and the rapid emergence of mutations, it is impossible to respond immediately using the current drug development processes. Therefore, the development of a new drug discovery method is necessary to overcome this problem and allow the quick discovery of antiviral drugs. Another example is the unmet need to increase the bioactivity of implant materials. Although biocompatibility is essential to prevent adverse effects following the implantation of external materials into the body, bioactivity, which described interactions between the prosthetic material and biological components, is more critical in securing the long-term stability of prosthetic materials. Thus, many studies are being conducted to increase bioactivity by controlling the surface properties of the implant material in various ways. Nevertheless, compared to minutely controlling

the thickness and roughness of its oxide film, there is a continuing need for a modification method that is somewhat simpler.

Nanobiotechnology refers to the combination of nanotechnology, which involves the development of new materials by identifying their physical properties at the atomic or molecular level, and biotechnology, which refers to the study of life phenomena. Nanobiotechnology can be applied to solve biological and biotechnological problems unsolvable by classical approaches. Therefore, the core goal of nanobiotechnology is to develop new nanomaterials with excellent properties that can be applied to various fields such as biosensors, biochips, drug delivery, therapeutics, and tissue regeneration.

Graphene oxide (GO) is an attractive nanomaterial due to its excellent physicochemical properties, originating from its oxygen functional groups and sp^2 carbon domains. As a representative feature, GO can quench fluorescent molecules located within 20 nm by adsorption. Therefore, GO is being used in research on various fluorescence-based biosensors. In addition, because GO has excellent biocompatibility and bioactivity to induce bone regeneration and cell differentiation, it is being used in regenerative medicine and prosthetic research.

Herein, we suggest a solution to the problems mentioned above using GO. First, we will address the development of a drug screening platform for rapid antiviral drug discovery: We developed a graphene oxide-based RNA viral helicase assay named RheGO. This assay could be used to analyze helicase activity in real-time with excellent reproducibility and reliability, and was applicable to antiviral drug screening. The antiviral activity of the hit compound identified with RheGO was also confirmed *in vitro* and *in vivo*.

Second, we will address the need to improve the bioactivity of implant materials:

We coated GO on the surface of the implant material with simple processing. As a result, we confirmed that the adhesion and proliferation of gingival fibroblasts increased when GO was coated. Moreover, we confirmed that the expression of focal adhesion genes was increased when gingival fibroblasts came into contact with GO.

Thus, we showed that problems that were difficult to solve with classical methods could be solved with new approaches using nanobiotechnology. Moreover, we believe that many medical and biotechnology problems can potentially be solved using GO to develop new methods for antiviral drug discovery and new materials with excellent bioactivity.

Keywords : Nanobiotechnology, Graphene Oxide, Biosensor, High-throughput Assay, Antiviral Drug Discovery, Bioactive Material, Dental implant

Student Number : 2014‐21257

Table of Contents

List of Figures

Chapter 1. Introduction

Chapter 2. Identification of a Direct-acting Antiviral Agent Targeting RNA Helicase via a Graphene Oxide Nanobiosensor

Chapter 3. Graphene Oxide-treated Surface of Pure Titanium Promotes Adhesion and Proliferation of Human Gingival Fibroblast

Chapter 1. Introduction

1.1 Graphene Oxide: its Applications as Biosensor and Bioactive material

Graphene is 2D honeycomb-like structure composed by single sp^2 carbon layer, which was first isolated from graphite in 2004.[1] It has drawn much attention from numerous researchers due to its unique physical/chemical properties such as high planar surface area, superior mechanical strength, thermal/electrical conductivity and optical property.[2] The intrinsic properties of graphene have driven many researchers to apply graphene to various research fields, including energy storage, sensor, transparent electrode, etc.[3-8]

Meanwhile, graphene oxide (GO) has also received attentions as well as graphene, for its various biomedical applications including biosensors.[9-19] GO is literally the oxidized derivative of graphene,[19-20] where the graphene-like 2D carbon sheet structure and various oxygen functional groups such as epoxy, carboxyl, carbonyl, hydroxyl group coexist. In addition, these functional groups may be placed at either the basal plane or edge of the sheet structure.[21-23] GO could be synthesized by oxidizing graphite with strong acid. There have been various synthesis protocols established for GO. In 1859, Brodie first reported a methodology for synthesis of graphene oxide from graphite by treating potassium chlorate and fuming nitric acid.[24] Staudenmaier[25] and Hofmann[26] also suggested the modified synthesis method of graphene oxide by changing acid compounds. One of the most common synthesis method to prepare GO was proposed by Hummers in 1957,[27] also known as the Hummer's method. By using sulfuric acid, sodium nitrate and potassium permanganate, this method required shorter time, lower

reaction temperature than other previous methods. Recently, various modified methods to synthesize GO based on Hummers' method have been reported. [28-30]

The 2-D single layer sheet structure and oxygen functional groups of GO enable the maintenance of similar physicochemical properties from the various synthesis methodologies. Such properties include amphiphilicity,[31] stability in aqueous solutions,[32] strong adsorption of certain molecules onto GO plane through π- π stacking[33] and hydrogen bonding,[34] and facile surface modification with various molecules. [35-41] GO may also serve as a fluorescence quencher, involving the adsorption process of dye molecule on GO plane, followed by fluorescence resonance energy transfer (FRET) to result in quenching of the fluorescence signal.[42] GO can absorb laser light energy and transfer the energy to other molecules on its surface.[43] Moreover, GO not only enhances Raman signal by chemical enhancement mechanism on its surface,[44] but also has peroxidase-like catalytic activity.[45] In addition, GO has electroactive property which enable reversible electrical reduction and oxidation.[46] Furthermore, GO is precursor of reduced GO (rGO) prepared by treating GO with reducing agent. [47-49] rGO shows better conductivity than GO.[50]

Due to its intrinsic properties, GO has enabled the development of various types of biosensor incorporating electrochemical, optical (fluorescence, colorimetric and Raman), and mass analysis. Yet, strategies only based on the basic properties of GO have been restricted to the detection of simple targets such as nucleic acids and small molecules. Recent studies have given priority to adaptation of biochemical properties of other functional materials along with GO to overcome restricted applications. As a result, there was the expansion of research about GO biosensor.

Moreover, GO has excellent biocompatibility, and can be used as a drug carrier

or nanomedicine.[51, 52] Additionally, it is also a bioactive material that can promote various biological responses.[53] For example, GO induce osteogenic differentiation of stem cell due to providing cytoskeletal tension.[54] Further, it can promote angiogenesis because of produces low-level reactive oxygen species.[55] In addition, GO can increase cell proliferation by enhancing the expression of focal adhesion genes.[56] Therefore, there is no doubt that GO is a promising bioactive material that can be used for bone tissue engineering and prosthetic implants.

Here, we introduce a FRET-based GO biosensor for a viral enzyme to identify a novel inhibitor, and a method to improve the bioactivity of implant material, pure titanium, with GO.

1.2 Description of Research

1.2.1 Identification of a Direct-acting Antiviral Agent Targeting RNA Helicase via a Graphene Oxide Nanobiosensor

Dengue virus (DENV), an arbovirus transmitted by mosquitoes, causes infectious diseases such as dengue fever, dengue hemorrhagic fever, and dengue shock syndrome. Despite the dangers posed by DENV, there are no approved antiviral drugs for treatment of DENV infection. Considering the potential for a global dengue outbreak, rapid development of antiviral agents against DENV infections is crucial as a preemptive measure; thus, the selection of apparent drug targets, such as the viral enzymes involved in the viral life cycle, is recommended. Helicase, a potential drug target in DENV, is a crucial viral enzyme that unwinds double-stranded viral RNA, releasing single-stranded RNA genomes during viral replication. Therefore, an inhibitor of helicase activity could serve as a direct-acting antiviral agent.

Here, we introduce **R**NA **he**licase assay based on **G**raphene **O**xide (RheGO), which enables fluorescence-based analysis of RNA substrate-specific helicase enzyme activity. This assay demonstrated high reliability and ability for high-throughput screening, identifying a new helicase inhibitor candidate, micafungin (MCFG), from an FDA-approved drug library. As a direct-acting antiviral agent targeting RNA helicase, MCFG inhibits DENV proliferation in cells and an animal model. Notably *in vivo*, MCFG treatment reduced viremia, inflammatory cytokine levels, and viral loads in several tissues and improved survival rates by up to 40% in a lethal mouse model. Therefore, we suggest MCFG as a potential direct-acting antiviral drug candidate.

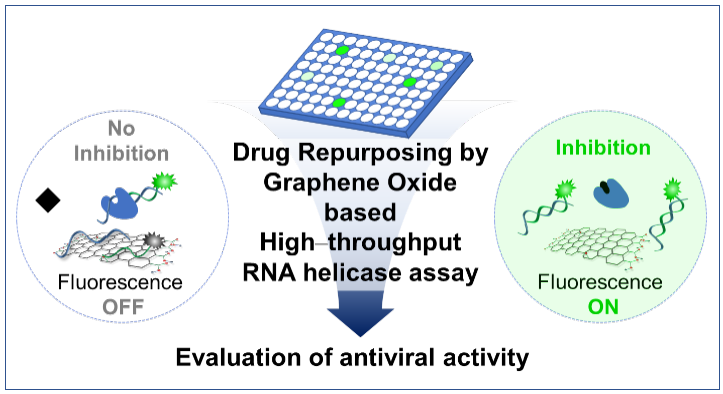

Figure 1.2.1 A strategy for viral RNA helicase assay and its application to antiviral drugs screening

1.2.2 Graphene Oxide-treated Surface on Pure Titanium Implant Materials Promotes Adhesion and Proliferation of Human Gingival Fibroblast

Dental implantation is the most common method for resolving tooth loss caused by disease or trauma. To increase the durability of the dental implants currently available, it is necessary to increase the bioactivity of the implant material. This can be done by changing the chemical properties of the surface through surface fabrication using nanomaterials such as graphene oxide (GO). GO consists of nanosized graphene domains and oxygen functional groups, can improve cellular properties including cell adhesion and proliferation.

In this study, we confirmed the bioactivity of GO-coated titanium in human gingival fibroblasts. It was observed that GO coating did not affect the roughness of titanium. Moreover, cell adhesion on titanium substrates was enhanced because the expression of related genes was initially elevated owing to the GO coating. It was also confirmed that GO-coated implants showed excellent bioactivity by improving cell proliferation. Therefore, GO can be used as a coating material in implants as well as in tissue engineering to improve cellular responses.

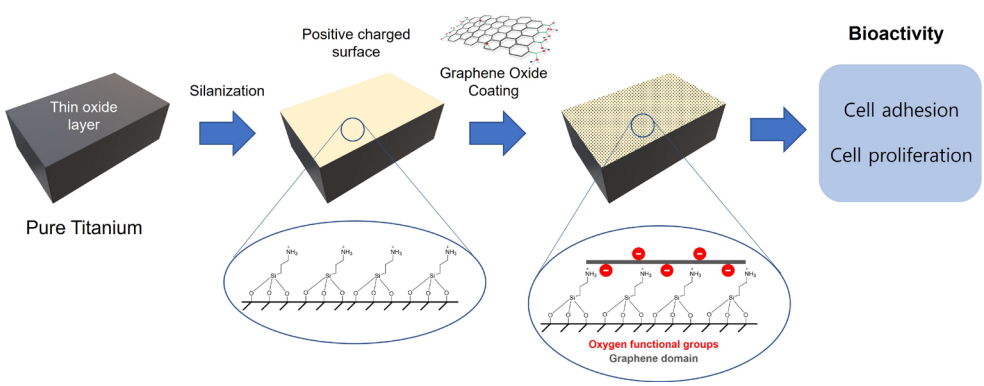

Figure 1.2.2 A strategy for enhancing bioactivity of implant material

1.3 References

1. Novoselov, K. S.; Geim, A. K.; Morozov, S. V.; Jiang, D.; Zhang, Y.; Dubonos, S. V.; Grigorieva, I. V.; Firsov, A. A. *Science* **2004**, *306*, 666-669.
2. Allen, M. J.; Tung, V. C.; Kaner, R. B. *Chem. Rev.* **2010**, *110*, 132-145.
3. Raccichini, R.; Varzi, A.; Passerini, S.; Scrosati, B. *Nat. Mater.* **2015**, *14*, 271-279.
4. Liu, Y.; Dong, X.; Chen, P. *Chem. Soc. Rev.* **2012**, *41*, 2283-307.
5. Kim, K. S.; Zhao, Y.; Jang, H.; Lee, S. Y.; Kim, J. M.; Kim, K. S.; Ahn, J. H.; Kim, P.; Choi, J. Y.; Hong, B. H. *Nature* **2009**, *457*, 706-710.
6. Choi, W.; Lahiri, I.; Seelaboyina, R.; Kang, Y. S. *Crit. Rev. Solid. State.* **2010**, *35*, 52-71.
7. Moon, J. S. *Carbon Lett.* **2012**, *13*, 17-22.
8. Zhang, Y.; Zhang, L. Y.; Zhou, C. W. *Acc. Chem. Res.* **2013**, *46*, 2329-2339.
9. Yin, P. T.; Shah, S.; Chhowalla, M.; Lee, K. B. *Chem. Rev.* **2015**, *115*, 2483-531.
10. Bitounis, D.; Ali-Boucetta, H.; Hong, B. H.; Min, D. H.; Kostarelos, K. *Adv. Mater.* **2013**, *25*, 2258-68.
11. Chung, C.; Kim, Y. K.; Shin, D.; Ryoo, S. R.; Hong, B. H.; Min, D. H. *Acc. Chem. Res.* **2013**, *46*, 2211-2224.
12. Lee, J.; Kim, J.; Kim, S.; Min, D. H. *Adv. Drug. Deliv. Rev.* **2016**, *105*, 275-287.
13. Loh, K. P.; Bao, Q.; Eda, G.; Chhowalla, M. *Nat. Chem.* **2010**, *2*, 1015-24.
14. Gao, L.; Lian, C.; Zhou, Y.; Yan, L.; Li, Q.; Zhang, C.; Chen, L.; Chen, K. *Biosens. Bioelectron.* **2014**, *60*, 22-29.

15. Bogue, R. *Sensor Review* **2014**, *34*, 233-238.

16. Ge, S.; Lan, F.; Yu, F.; Yu, J. *New J. Chem.* **2015**, *39*, 2380-2395.

17. Morales-Narvaez, E.; Merkoci, A. *Adv. Mater.* **2012**, *24*, 3298-308.

18. Nurunnabi, M.; Parvez, K.; Nafiujjaman, M.; Revuri, V.; Khan, H. A.; Feng, X.; Lee, Y.-k. *RSC Adv.* **2015**, *5*, 42141-42161.

19. Yoo, J. M.; Kang, J. H.; Hong, B. H. *Chem. Soc. Rev.* **2015**, *44*, 4835-52.

20. Huang, X.; Yin, Z.; Wu, S.; Qi, X.; He, Q.; Zhang, Q.; Yan, Q.; Boey, F.; Zhang, H. *Small* **2011**, *7*, 1876-902.

21. Hunt, A.; Dikin, D. A.; Kurmaev, E. Z.; Boyko, T. D.; Bazylewski, P.; Chang, G. S.; Moewes, A. *Adv. Funct. Mater.* **2012**, *22*, 3950-3957.

22. Gao, W.; Alemany, L. B.; Ci, L.; Ajayan, P. M. *Nat. Chem.* **2009**, *1*, 403-408.

23. Kang, J. H.; Kim, T.; Choi, J.; Park, J.; Kim, Y. S.; Chang, M. S.; Jung, H.; Park, K. T.; Yang, S. J.; Park, C. R. *Chem. Mater.* **2016**, *28*, 756-764.

24. Brodie, B. C. *Phil. Trans. R. Soc. Lond.* **1859,** *149*, 249-259

25. Staudenmaier, L. *Ber. Dtsch. Chem. Ges.* **1898**, *31*, 1481−1487

26. Hofmann, U.; Konig, E. *Z. Anorg. Allg. Chem.* **1937**, *234*, 311−336

27. Hummers, W. S.; Offeman, R. E. *J. Am. Chem. Soc.* **1958**, *80*, 1339-1339.

28. Zhang, L.; Li, X.; Huang, Y.; Ma, Y. F.; Wan, X. J.; Chen, Y. S. *Carbon* **2010**, *48*, 2367-2371.

29. Marcano, D. C.; Kosynkin, D. V.; Berlin, J. M.; Sinitskii, A.; Sun, Z. Z.; Slesarev, A.; Alemany, L. B.; Lu, W.; Tour, J. M. *ACS Nano* **2010**, *4*, 4806-4814.

30. Chen, J.; Yao, B. W.; Li, C.; Shi, G. Q. *Carbon* **2013**, *64*, 225-229.

31. Kim, J.; Cote, L. J.; Kim, F.; Yuan, W.; Shull, K. R.; Huang, J. X. *J. Am. Chem.*

Soc. **2010**, *132*, 8180-8186.

32. Shih, C. J.; Lin, S. C.; Sharma, R.; Strano, M. S.; Blankschtein, D. *Langmuir* **2012**, *28*, 235-241.

33. Su, Q.; Pang, S. P.; Alijani, V.; Li, C.; Feng, X. L.; Mullen, K. *Adv. Mater.* **2009**, *21*, 3191-3195.

34. Park, J. S.; Na, H. K.; Min, D. H.; Kim, D. E. *Analyst* **2013**, *138*, 1745-1749.

35. Liu, Z.; Robinson, J. T.; Sun, X. M.; Dai, H. J. *J. Am. Chem. Soc.* **2008**, *130*, 10876-10877.

36. Huang, P.; Xu, C.; Lin, J.; Wang, C.; Wang, X. S.; Zhang, C. L.; Zhou, X. J.; Guo, S. W.; Cui, D. X. *Theranostics* **2011**, *1*, 240-250.

37. Kim, Y. K.; Kim, M. H.; Min, D. H. *Chem. Commun.* **2011**, *47*, 3195-3197.

38. Georgakilas, V.; Tiwari, J. N.; Kemp, K. C.; Perman, J. A.; Bourlinos, A. B.; Kim, K. S.; Zboril, R. *Chem. Rev.* **2016**, *116*, 5464-5519.

39. Shao, J. J.; Lv, W.; Yang, Q. H. *Adv. Mater.* **2014**, *26*, 5586-5612.

40. Dreyer, D. R.; Park, S.; Bielawski, C. W.; Ruoff, R. S. *Chem. Soc. Rev.* **2010**, *39*, 228-40.

41. Wang, Y.; Li, Z.; Wang, J.; Li, J.; Lin, Y. *Trends Biotechnol.* **2011**, *29*, 205-12.

42. Kim, J.; Cote, L. J.; Kim, F.; Huang, J. X. *J. Am. Chem. Soc.* **2010**, *132*, 260-267.

43. Dong, X. L.; Cheng, J. S.; Li, J. H.; Wang, Y. S. Anal. Chem. **2010**, *82*, 6208-6214.

44. Yu, X. X.; Cai, H. B.; Zhang, W. H.; Li, X. J.; Pan, N.; Luo, Y.; Wang, X. P.; Hou, J. G. *ACS Nano* **2011**, *5*, 952-958.

45. Song, Y.; Qu, K.; Zhao, C.; Ren, J.; Qu, X. *Adv. Mater.* **2010**, *22*, 2206-10.

46. Ekiz, O. O.; Urel, M.; Guner, H.; Mizrak, A. K.; Dana, A. *ACS Nano* **2011**, *5*,

2475-2482.

47. Si, Y.; Samulski, E. T. *Nano Letters* **2008**, *8*, 1679-1682.

48. Park, S.; An, J. H.; Jung, I. W.; Piner, R. D.; An, S. J.; Li, X. S.; Velamakanni, A.; Ruoff, R. S. *Nano Letters* **2009**, *9*, 1593-1597.

49. Shen, J.; Hu, Y.; Shi, M.; Lu, X.; Qin, C.; Li, C.; Ye, M. *Chem. Mater.* **2009**, *21*, 3514-3520.

50. Pei, S. F.; Cheng, H. M. *Carbon* **2012**, *50*, 3210-3228.

51. Kiew, S. F.; Kiew, L. V.; Lee, H. B.; Imae, T.; Chung, L. Y., *J Control Release* **2016,** *226*, 217-28.

52. Shareena, T. P. D.; McShan, D.; Dasmahapatra, A. K.; Tchounwou, P. B., *Nano-Micro Lett* **2018,** *10* (3).

53. Cheng, J. Y.; Liu, J. H.; Wu, B.; Liu, Z. Y.; Li, M.; Wang, X.; Tang, P. F.; Wang, Z., *Front Bioeng Biotech* **2021,** *9*.

54. Nayak, T. R.; Andersen, H.; Makam, V. S.; Khaw, C.; Bae, S.; Xu, X. F.; Ee, P. L. R.; Ahn, J. H.; Hong, B. H.; Pastorin, G.; Ozyilmaz, B., *Acs Nano* **2011,** *5* (6), 4670-4678.

55. Mukherjee, S.; Sriram, P.; Barui, A. K.; Nethi, S. K.; Veeriah, V.; Chatterjee, S.; Suresh, K. I.; Patra, C. R., *Adv Healthc Mater* **2015,** *4* (11), 1722-1732.

56. Ryoo, S. R.; Lee, J.; Yeo, J.; Na, H. K.; Kim, Y. K.; Jang, H.; Lee, J. H.; Han, S. W.; Lee, Y.; Kim, V. N.; Min, D. H. *ACS Nano* **2013**, *7*, 5882-5891.

Chapter 2. Identification of a Direct-acting Antiviral Agent Targeting RNA Helicase via a Graphene Oxide Nanobiosensor

2.1 Introduction

Viral infectious diseases post a significant threat to human health.[1] However, vaccine development and improvements in hygiene have significantly contributed to the partial suppression of emerging viral diseases. Nevertheless, little success has been achieved in controlling viral epidemics, as evidenced by the outbreak of severe acute respiratory syndrome in 2002, Ebola in 2013, middle-Eastern respiratory syndrome and Zika in 2015,[2] and COVID 19.[3,4]

Dengue fever (DF) is a prominent infectious viral disease, with 50 million infections reported annually, including 500,000 hospitalizations for dengue hemorrhagic fever or dengue shock syndrome, with a fatality rate of 2.5%. The causative agent of DF is the dengue virus (DENV), a mosquito-borne single positive-stranded RNA virus of the family Flaviviridae.[5,6] Given that advances in transportation systems have accelerated the spread of DENV globally, it has now been disseminated to more than 100 countries in Southeast Asia, the western Pacific, Europe, and North and South Americas.[5,6] Nevertheless, there are limited treatments for DENV such as supportive care, with no approved drugs.[7]

Nucleoside analogs and chemical drugs targeting host enzymes have been previously investigated.[8-10] However, the harmful adverse effects of these strategies, such as metabolic disorders, hindered the development of antiviral agents;[11,12] for example, Celgosivir, which targets the host enzyme α-glucosidase, is recommended for the short-term treatment of DENV owing to its intrinsic toxicity,[13] while

NITD008, a nucleoside analog, did not proceed to clinical trials owing to the significant side effects observed during preclinical studies.[14] The development of direct-acting antiviral agents (DAAs) can be an effective strategy to overcome the limitations of conventional antiviral drug development methodologies. DAAs are a novel class of drugs that target specific stages in the viral life cycle; the working mechanisms of these drugs provide them with high eradication rates and excellent safety profiles.[15,16]

One of the major challenges in antiviral discovery is its tedious and time-consuming stages, which is not enough to prevent the rapid spread of the virus. Drug repurposing has been proposed as a breakthrough to accelerate the drug development process. The concept of drug repurposing is to assign approved drugs to new indications. Thus, repurposed drugs can easily enter clinical trials and may even bypass phase I clinical studies, shortening the time required for a potential antiviral agent to reach clinical applications.[17,18] Therefore, the development of DAAs through repurposing can be an effective approach to discover potential antiviral candidates and reduce their developmental period.

The main targets of DAAs are virus-encoded proteins that are crucial for viral replication, such as helicase, which is involved in the viral replication cycle and unwinds double-stranded RNA to release single-stranded RNA viral genomes.[19-22] To discover DAAs targeting helicase, a number of high-throughput screening (HTS) strategies have been introduced, based on various assays, including nucleic binding, ATPase, and thermo-shift assays.[23-26] However, since these assays detect binding with nucleic acid, interference with hydrolysis or binding of ATP, and interactions between proteins and drugs, rather than whole unwinding activities, they remain limited. Therefore, it is essential to screen drugs against the enzymes'

activities, which can provide various inhibition sites. Conventional unwinding activity assays are limited; for example, the conventional gel-shift assay is labor-intensive and time-consuming. The molecular beacon assay is another conventional method with high potential, however, there have been several concerns regarding its low selectivity due to signal interference. Therefore, these conventional methods are not suitable for developing DAAs targeting helicase.[27,28]

Previously, we described a new and simple helicase assay, graphene oxide (GO)-based helicase assay, that produced robust results.[29,30] Since GO has a high affinity for nucleobases and fluorescence-quenching ability, it enables convenient fluorescence-based analysis. However, this assay was designed using a thoroughly studied viral helicase model, the hepatitis C virus (HCV) NS3, which exhibits high *in vitro* unwinding activity on the DNA substrate despite the genome of HCV being a single-stranded RNA.[31-33] Considering that typical viral RNA helicases, including the DENV helicase, recognize RNA as a substrate,[34,35] improvements are required to utilize this system as a general RNA helicase activity assay.

Here, we present an advanced GO-based helicase assay, referred to as the RNA helicase assay based on GO (RheGO). We demonstrated that RheGO, a fluorescence-based assay, provides robust results and is suitable for antiviral drug screening. Using RheGO, we performed high-throughput screening against a Food and Drug administration (FDA)-approved drug library and identified micafungin (MCFG), an antifungal agent, as a potent DENV helicase inhibitor. Moreover, MCFG showed significant antiviral efficacy in both cells and animal models. MCFG treatment significantly inhibited DENV proliferation in Vero E6 cells. Using dengue mouse models, we found that MCFG also decreased viremia, inflammatory cytokine levels, and viral loads in tissues as well as increased the

survival rate. Collectively, we suggest that MCFG can be a promising DAA candidate against DENV.

2.2 Results

Evaluation of *in vitro* unwinding activity of DENV helicase

Before establishing the GO-based helicase assay, we examined the *in vitro* activity of the DENV helicase prepared from NS3 by cloning and expressing the enzyme in *E. coli* (Figure 2.2.1A). Unlike the HCV helicase, the DENV helicase exhibits poor *in vitro* unwinding activity on the dsDNA substrate. Therefore, it is essential to obtain an optimal nucleic acid substrate to improve the unwinding activity of the DENV helicase. As demonstrated previously, when DENV helicase binds to RNA as the major strand, excellent *in vitro* unwinding activity was observed, regardless of the type of the minor strand, i.e., DNA or RNA. Therefore, we prepared a helicase substrate consisting of an RNA as a major strand and a fluorescent dye-modified DNA minor strand (Figure 2.2.1B). With the prepared DENV helicase and substrate, we performed a conventional gel-shift assay (Figure 2.2.1C) and demonstrated that the presence of helicase in the reaction mixture generated ssDNA; the helicase released ssDNA when ATP, the energy source for helicase, was added to the reaction mixture (Figure 2.2.1C lanes 5 and 6). Moreover, the amount of ssDNA was directly proportional to the concentration of the helicase (Figure 2.2.1C lanes 6–8).

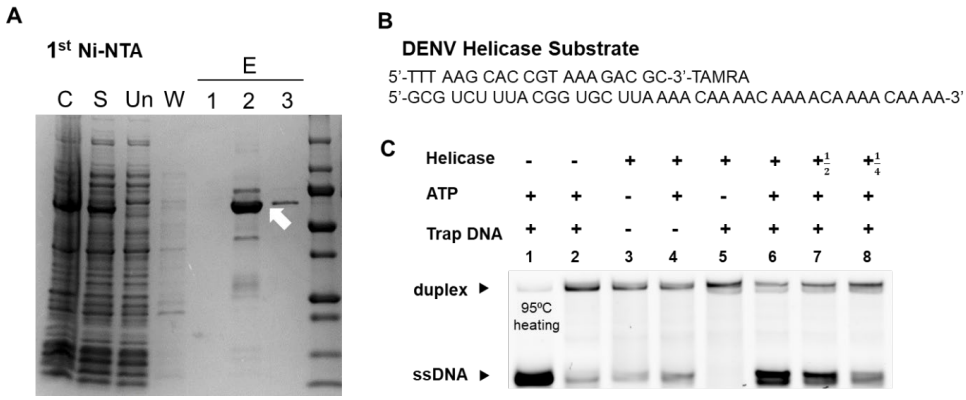

Figure 2.2.1 Expression of DENV helicase and confirmation of its in vitro unwinding activity.

(A) SDS-PAGE image for 1st Ni-NTA purification of DENV helicase from E.coli lysate (white arrow). Each lane represents the sample obtained during the protein purification process. Samples were abbreviated as follows; C: Cell lysate, S: Soluble protein, Un: Unbound flowthrough, W: Washed flowthrough with 40 mM imidazole containing buffer, and E 1/2/3: Eluted fractionation with 200mM imidazole containing buffer. (B) TAMRA labeled DENV helicase substrate sequence. (C) Analysis of unwinding activity for dengue helicase (lane 6, 7 and 8 ; [helicase] = 78, 39 and 19.5 nM) based on native-gel shift assay.

Development of GO-based RNA helicase assay (RheGO)

Based on the data obtained from previous experiments, we developed a fluorescence-based DENV helicase assay platform, RheGO, consisting of RNA substrate and GO. RheGO is based on the physicochemical properties of GO, which has a hexagonal sp^2 carbon domain and oxygen-containing chemical functional groups, thus enabling GO to interact strongly with aromatic molecules, including nucleobases and chemical dyes, via π-π interactions and hydrogen bonds. GO can also quench fluorescence from chemical dyes via fluorescence resonance energy transfer.[36,37] Owing to these properties, we hypothesized that GO is utilized in RheGO as a scavenger of single-stranded nucleic acids with exposed nucleobases and as a quencher of fluorescent dyes. Thus, using fluorescent dye-modified double-stranded nucleic acid substrates and GO, the helicase activity (i.e., unwinding of double-stranded substrate into single strands) could be examined using fluorescent signals.

As one of the major components of RheGO, GO was synthesized using the modified Hummers' method.[38] The single-layered structure of the GO sheet was analyzed using atomic force microscopy (AFM) (Figure 2.2.2A). The height profile displayed GO sheets with a thickness of approximately 1 nm. Fourier-transform infrared spectroscopy (Figure 2.2.2B) revealed C=O and C-O stretching peaks at 1,728 and 1,049 cm^{-1}, respectively, indicating oxygen-containing functional groups. In addition, Raman spectroscopy detected a D peak attributed to structural disorder and a G peak related to the ordered sp^2 domain at 1,350 and 1,605 cm^{-1}, respectively (Figure 2.2.2C).

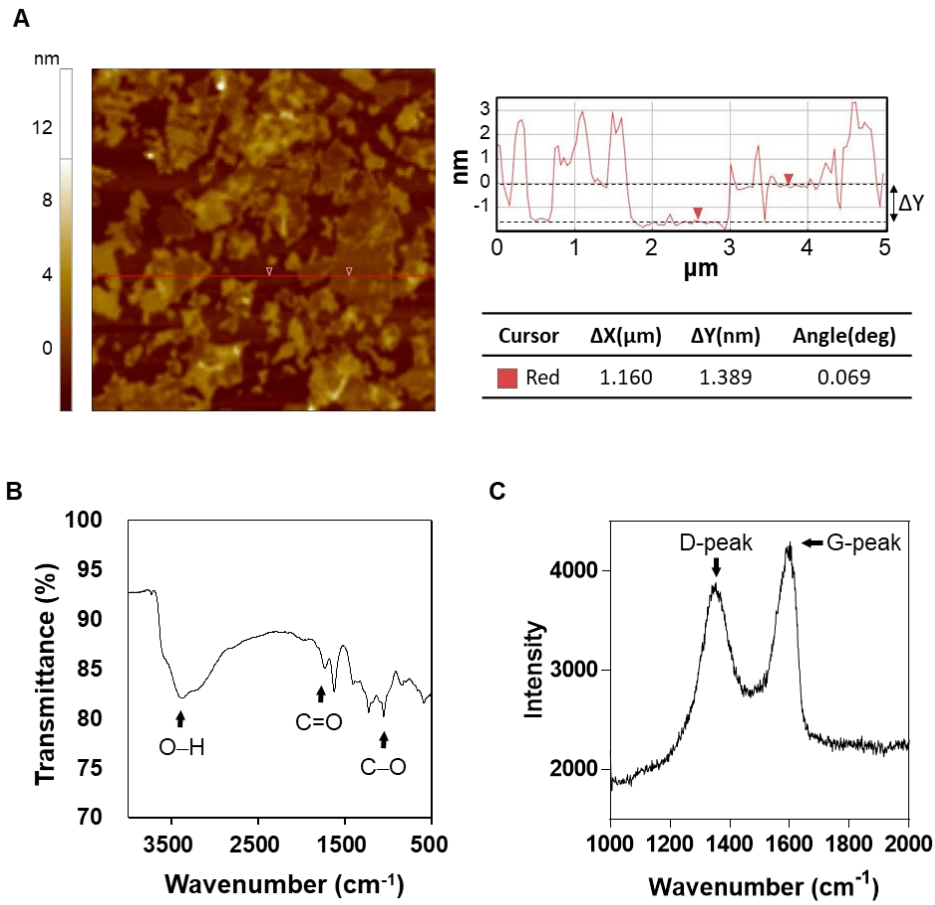

Figure 2.2.2 Characterization of graphene oxide (GO).

(A) The surface morphology image and height profile of GO are observed by AFM.

(B) Oxygen-containing chemical functional groups of GO are analyzed by FT-IR.

(C) D- and G-peak from GO are determined by Raman spectroscopy.

Next, we performed RheGO and found that the fluorescence signal changed, showing an emission at 570 nm (Figure 2.2.3A). The negative control (0 nM) showed slightly decreased fluorescence signals; however, a plateau with high signal was soon reached. The addition of helicase decreased the fluorescence signal over time, and the rate of signal reduction increased in a helicase concentration-dependent manner. The concentration-dependent result correlated with the gel-shift assay outcomes (Figure 2.2.1C lanes 6-8). Using RheGO, we found a significant difference in fluorescence intensity between the reaction mixtures with and without 26 nM helicase within 50 min.

Additionally, we determine whether RheGO could detect enzyme inhibition when an enzyme inhibitor is added. Given that ATP is the energy source for helicase, adenylyl-imidodiphosphate (AMP-PNP), a non-hydrolysable ATP analog, can serve as a model inhibitor of helicase activity. Therefore, we performed RheGO with the addition of various concentrations of AMP-PNP (Figure 2.2.3B) and observed a dose-response inhibition effect. We calculated the half-inhibitory concentration (IC_{50}) value to be approximately 20 mM.

Finally, to verify the feasibility of RheGO as an inhibitor screening platform, we examined its robustness. First, we obtained fluorescence images of multiple reaction mixtures. In the first row, the samples were prepared by varying the helicase concentrations in a 96-well plate. In the second row, the samples with various AMP-PNP concentrations were arranged. As expected, the fluorescence images showed that the fluorescence intensity of each well reflected the helicase activity and inhibitory activity quantitatively (Figure 2.2.3C). Meanwhile, as a statistical value that warrants the assay proposing high-throughput screening, the Z'-factor is commonly used.[39] A Z'-factor value from 0.5 to 1 indicates that the

assay is highly reliable. Our calculations showed that the Z'-factor of RheGO was 0.81 (Figure 2.2.3D), indicating that RheGO is suitable for high-throughput screening.

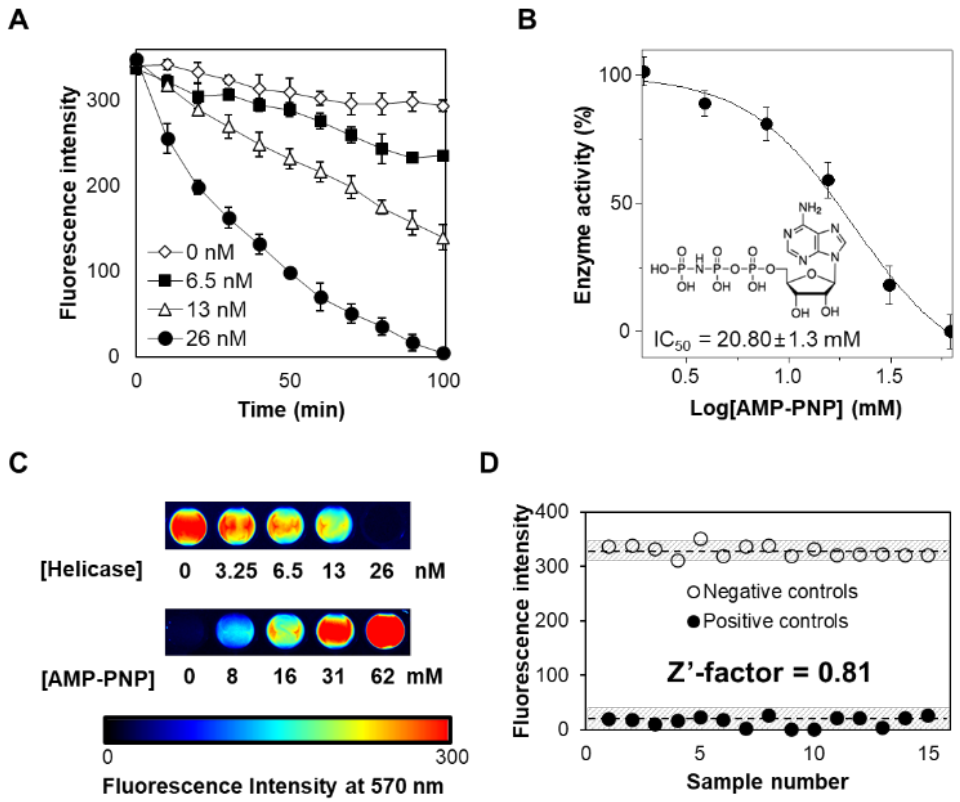

Figure 2.2.3 Performance validation of RheGO.

(A) Concentration-dependent monitoring of the helicase activity by RheGO. (B) Dose-dependent inhibition of the helicase with various concentrations of AMP-PNP added into RheGO. (C) Fluorescent images obtained from a concentration-dependent assay. Row 1: helicase addition; row 2: AMP-PNP addition. (D) Z'-factor analysis showing the reliability of the assay. Bars in all graphs indicate the ±SEM.

Screening helicase inhibitor from an FDA-approved drug library

We have thus far showed that RheGO can be used as a high-throughput screening platform for discovering DENV helicase inhibitors. Using RheGO, we performed high-throughput inhibitor screening against FDA-approved drug library consisting of 1,443 compounds. The brief procedures and results of this strategy, referred to drug repurposing, are as follows: First, to narrow down the range of inhibitor candidates rapidly, primary screening was executed (Figure 2.2.4A). We added 100 μM of each compound to RheGO plates in the primary screening step and then identified 41 compounds showing an inhibitory effect that exceeded 50% (Figure 2.2.4C). In addition, to remove false signals generated by interference between the compounds and other components apart from the helicase, we used a counter-screening (Figure 2.2.4B). The counter-screening involved a single strand substrate instead of the duplex substrate. In such circumstance, the RheGO system would always exhibit the quenched fluorescence. Compounds which disrupted the ordinary quenching was screened out. Throughout the counter-screening process, six valid inhibitor candidates were selected from the library. Using the ratio between the half maximal inhibitory and cytotoxicity concentrations we selected micafungin (MCFG), which showed the greatest suppression efficacy with an IC_{50} value of approximately 5 μM and the lowest cytotoxicity over 250 μM, as a hit compound (Figure 2.2.4D).

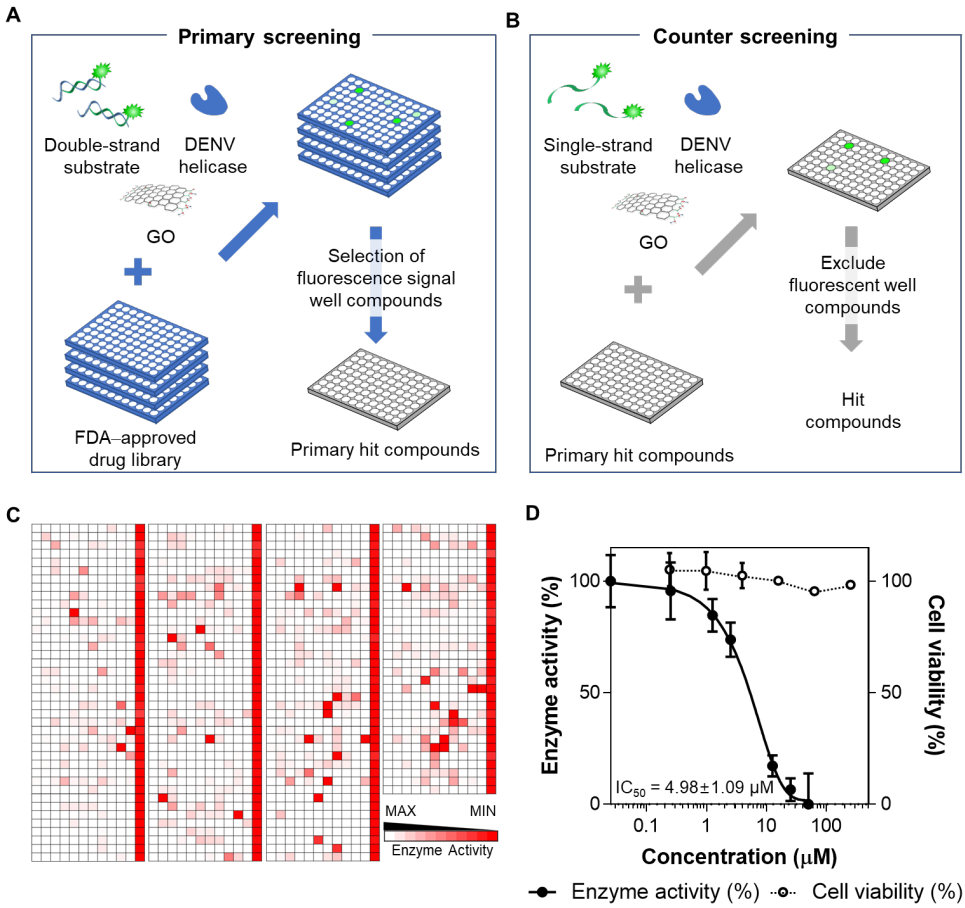

Figure 2.2.4 Strategy of drug repurposing and discovery of a DENV helicase inhibitor based on RheGO.

(A) Scheme for primary screening with RheGO. (B) Scheme of a counter-screening strategy to detect false-positive compounds, and (C) primary screening against 1,443 FDA-approved chemical compounds. Each plate contained replicated negative and positive controls in the first and last columns, respectively. (D) Dose-dependent inhibition of the dengue helicase and Cell (Vero E6) viability after treatment with various concentrations of MCFG. Calculated IC_{50} value for the hit compound is also shown. Bars in the graph indicate the ± SEM.

The hit compound micafungin showed *in vitro* antiviral activity in a cell-based assay

Owing to the inhibitory effect of MCFG against the DENV helicase, we expected that MCFG would exhibit antiviral activity in cell-based assays as well. Before the MCFG treatment to cells the cytotoxicity of MCFG was first evaluated (Figure 2.2.5A). MCFG did not show cytotoxicity at doses up to 300 μM in Vero E6 cells. Subsequently, to prove the antiviral effect of MCFG, a focus reduction assay was conducted (Figure 2.2.5B). We inoculated 100 focus forming units (FFU) of dengue virus serotype 2 (DENV2) with various MCFG concentrations into Vero E6 cells, then incubated them for 48 h. The formation of the viral focus was inhibited in a dose-responsive manner with a half-maximal effective concentration (EC50) of approximately 46 μM. Additionally, we analyzed the amount of viral RNA in the infected cells to confirm the MCFG antiviral efficacy (Figure 2.2.5C). After DENV2 was inoculated into Vero E6 cells at a multiplicity of infection of 0.1, MCFG was added at various concentrations. Real-time PCR analysis showed that the amount of viral RNA decreased as the MCFG concentration increased. At 38 μM MCFG treatment, approximately 50% reduction of viral RNA in cells was noted. Furthermore, immunofluorescence images revealed that the DENV antigen declined in a dose-responsive manner (Figure 2.2.5D).

To determine whether MCFG has similar antiviral activity on a human cell line, we performed the same experiments in Huh-7 cells, a human hepatoma-derived cell line. Based on the results of the experiments with Vero E6 cells, Huh-7 cells were treated with MCFG up to the maximum dosing concentration of 150 μM for 48 h; no substantial cytotoxicity was observed (Figure 2.2.5E). Furthermore, the expression level of viral RNA in DENV2-infected Huh-7 cells was correlated with

the MCFG concentration (Figure 2.2.5E). These results were further confirmed by immunofluorescence images, demonstrating a similar tendency to the effects on Vero E6 cells (Figure 2.2.5F).

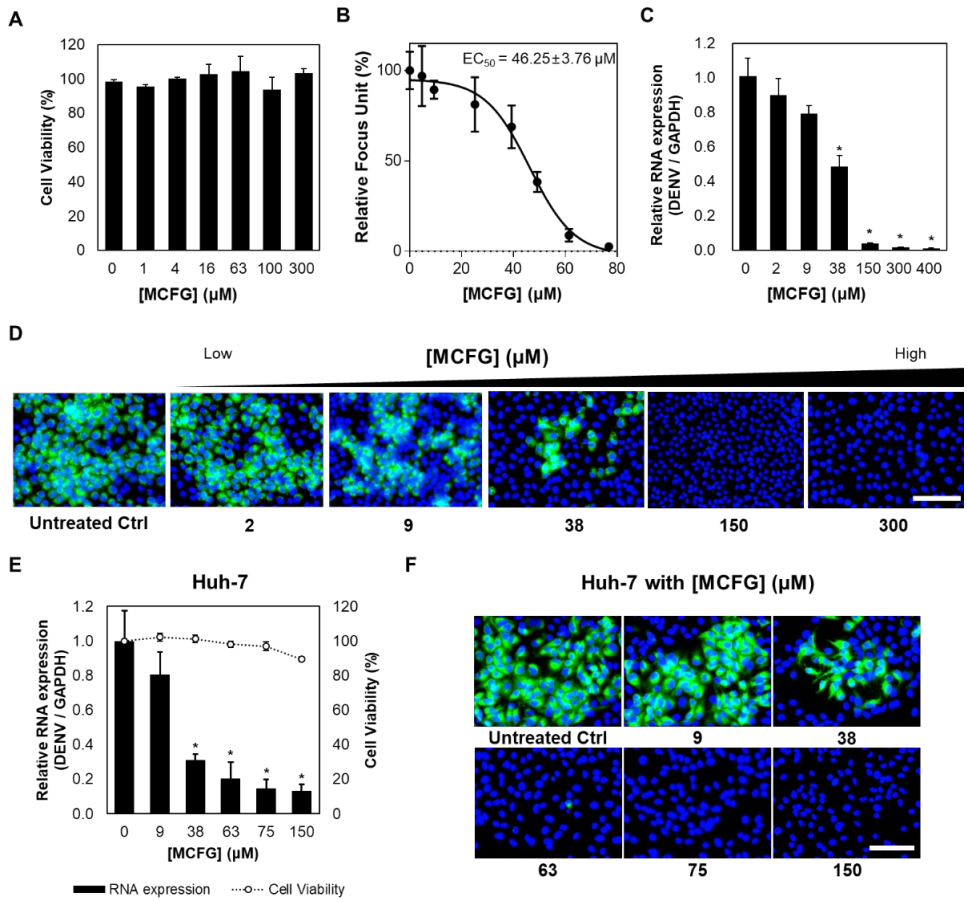

Figure 2.2.5 Cell-based antiviral evaluation of MCFG.

(A) Cell (Vero E6) viability after treatment with various concentrations of MCFG (n = 5). (B) Dose-dependent inhibition of DENV replication and the calculated EC_{50} value for MCFG (n = 5). (C) Relative reduction of DENV RNA expression by increasing the compound (MCFG) concentration (n = 3). Statistical significance was confirmed by Student's *t*-test; * denotes $p < 0.05$. (D) Immunofluorescent staining images of DENV-infected Vero E6 cells with various concentrations of MCFG. Blue, nucleus; green, DENV antigen. (E) Cell (Huh-7) viability after treatment with various concentrations of MCGF (n = 5) and the relative reduction of DENV RNA expression by increasing the compound concentration (n = 3).

Statistical significance was confirmed by Student's t-test. *p < 0.05. (F) Immunofluorescent staining images of DENV-infected Huh-7 cells treated with various concentrations of MCGF. Blue, nucleus; green, DENV antigen. Bars in graphs indicate the ± SEM. Scale bars represent 100 μm.

MCFG showed *in vivo* antiviral efficacy

As MCFG showed an antiviral effect *in vitro*, we subsequently evaluated its antiviral efficacy in an animal model using the AG129 mouse strain, which is a type I & II interferon receptor knockout transgenic mouse, which is commonly used to build the DENV-infected model. AG129 mouse is susceptible not only to non-adapted DENV but also to clinical strains of DENV.[40,41] We previously reported that intraperitoneal (i.p.) injection of a 1×10^7 FFU/mouse dose of DENV2 resulted in characteristic symptoms of DENV infection and increased mortality in infected mice.[42] Based on this report, we established a DENV infection mouse model.

We then assessed changes in pathological signs and symptoms following treatment with MCFG *in vivo*. Initially, we confirmed the peak viremia change according to the drug treatment (Figure 2.2.6A). At a dose of 75 mg/kg once a day, there was a significant (87%) decrease in the peak viremia level ($p < 0.05$), indicating that MCFG could reduce the viral load in the serum. Notably, the expression of inflammatory cytokines including tumor necrosis factor (TNF), interferon γ (IFN-γ), and interleukin 6 (IL-6) increase in mice when infected with DENV. We subsequently examined the changes in the levels of inflammatory cytokines in DENV-infected mice treated with MCFG using the same dose (Figure 2.2.6B) and found that the MCFG treatment reduced TNF, IFN-γ, and IL-6 levels by 2.0-, 2.2-, and 4.7-fold, respectively ($p < 0.05$).

The mice were sacrificed on day 3 post-infection and the representative organs

were collected for further analysis. First, the viral loads in the organ samples, specifically the spleen, liver, lung, large intestine, and small intestine were investigated through a real-time PCR analysis (Figure 2.2.6C). Overall, viral RNA was reduced in all the organs obtained from the MCFG-treated group. Although a significant decrease in the viral RNA was not observed in the spleen ($p = 0.0873$), MCFG treatment significantly reduced viral RNA in the liver, lung, large intestine, and small intestine by 2.1-, 8.7-, 4.4-, and 2.0-fold, respectively ($p < 0.05$). Moreover, there was a 1.5-fold reduction in the viral load in whole blood ($p < 0.05$). Additionally, histological alterations caused by DENV infection were examined in the liver, lung, and spleen.[41,43-45] Thus, tissue samples from the liver, lung, and spleen were fixed and embedded in paraffin. After staining the samples with hematoxylin and eosin (H&E), we assessed the specimens using an optical microscope (Figure 2.2.6E). Unlike in the phosphate buffered saline (PBS) group, focal necrosis was not observed in the MCFG treatment group in the liver. In addition, swelling of the alveolar septa in the lung due to DENV infection was diminished in the treatment group. The DENV-infected spleens showed a collapse of the boundary, referred to as the marginal zone, between white and red pulps. In the MCFG treatment group, the marginal zone was recovered.

Another pathological sign of DENV infection is splenomegaly. Hence, we investigated the weight and size of each spleen (Figure 2.2.6D and Figure 2.2.7) and found that the weight of the spleen in the DENV-infected group was significantly increased by 2.9-fold compared to that in the normal group ($p < 0.05$); in contrast, treatment with MCFG decreased the spleen weight by 1.4-fold compared to that in the infected mice ($p < 0.05$). Apart from these outcomes, increased spleen weights were also found in healthy mice treated with MCFG.

Although the expansion size was smaller by 0.5-fold than in the DENV-infected group, we confirmed, through a comparison with non-drug-treated healthy mice, that the spleen was indeed enlarged ($p < 0.05$).

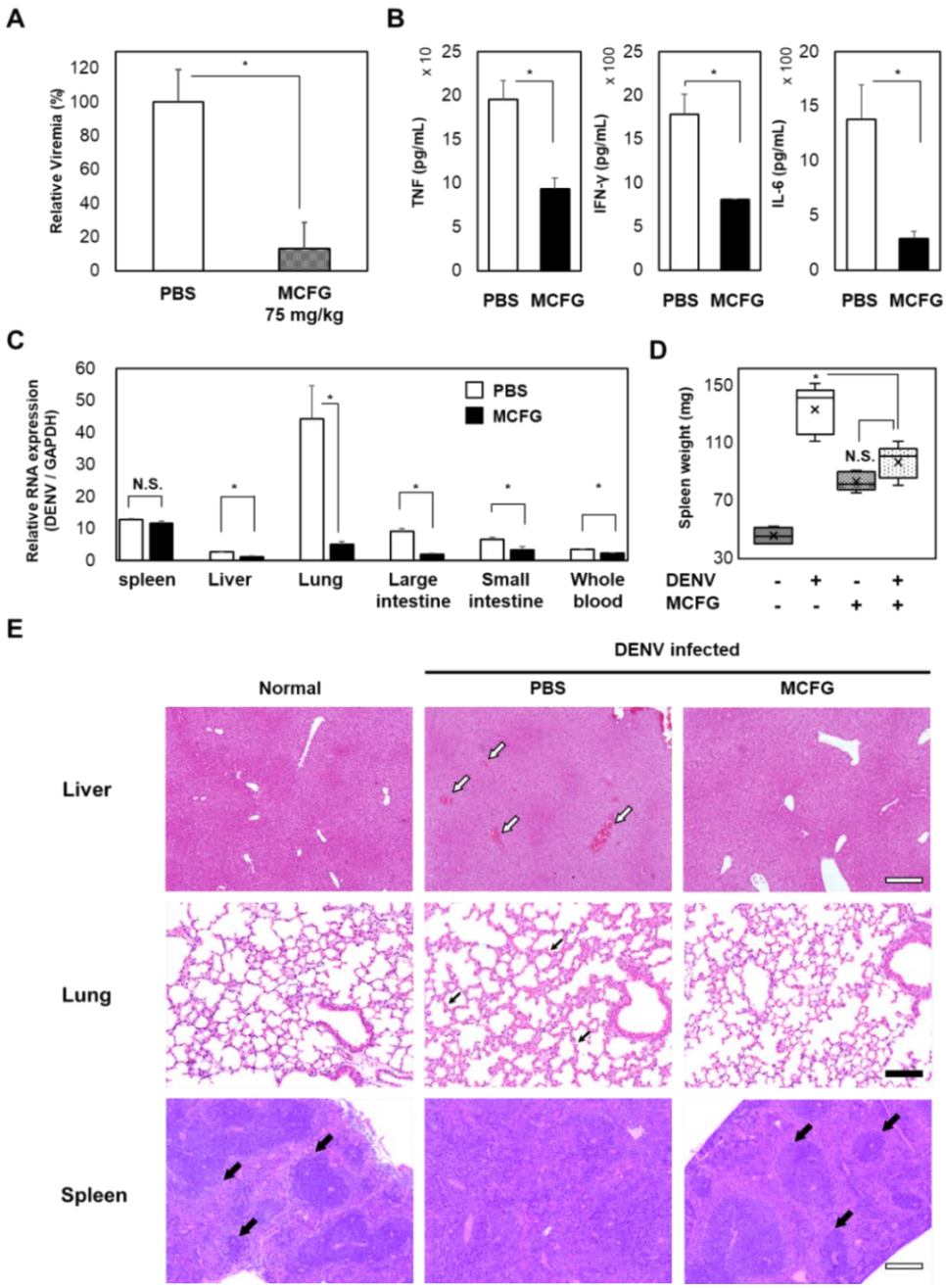

Figure 2.2.6 Antiviral activity of MCFG in DENV-infected AG129 mice.

MCFG was administered at a dose of 75 mg/kg i.p. once a day in all drug treatment

groups. Phosphate buffered saline (PBS) controls were also treated with a dosing schedule identical to that of the MCFG group. (A) Viremia analysis based on absolute quantification by real-time PCR (n = 3). (B) Serum cytokine analysis results from a cytometric bead array. The black bar represents the drug-treated group and the white bar is the PBS control group (n = 5). inflammatory cytokines including tumor necrosis factor, TNF; interferon γ. IFN-γ; interleukin 6, IL-6. (C) Analysis of viral RNA in each tissue sample by real-time PCR (n = 5). (D) Comparison of spleen weights (n = 5). (E) Hematoxylin and eosin (H&E) staining images for each experimental group. Scale bars represent 100 μm (black) and 200 μm (white). The white arrows indicate focal necrosis in the liver. The small black arrows represent swollen alveolar septa in the lung. The large black arrows indicate the marginal zone in the spleen. Statistical significance was confirmed by Student's t-test. Bars in all graphs indicate the ±SEM. Not significant (N.S.); * for $p < 0.05$.

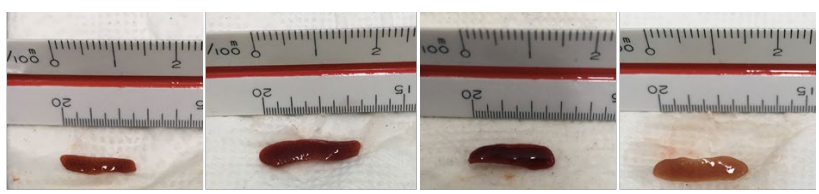

DENV	-	+	-	+
MCFG	-	-	+	+

Figure 2.2.7 Micafungin (MCFG) effect on splenomegaly induced by DENV infection in AG129 mice.

Furthermore, DENV infection contributes to hematological changes. Notably, acute viral infection induces leukopenia and lymphopenia. Hemorrhage, a severe disease manifestation, decreases the amount of red blood cells (RBC) in the blood.[41,46] To confirm the changes in each component, we analyzed blood samples from each group (Figure 2.2.8) and found that the changes in trends were similar to those described above with regard to white blood cells (WBC), lymphocytes, and RBC in DENV-infected mice. Though the changes were not significant in the MCFG treatment group, the WBC, lymphocyte, and RBC levels increased by 1.4-, 1.2-, and 1.1-fold, respectively ($p = 0.097$, 0.540, and 0.262, respectively). RBC level declined in normal mice treated with MCFG, although not significantly ($p = 0.314$).

Given that MCFG diminished the viral load and alleviated pathological signs, we further examined whether MCFG treatment would also reduce the DENV infection-derived mortality rate. We administered a dose of 1×10^7 FFU/mouse i.p. with DENV2 into 10 mice per group. For the drug treatment group, MCFG was administered once a day at a dose of 75 mg/kg upon the start of the infection. While the infected mice without drug treatment died within 10 days, 40% of those treated with MCFG survived (Figure 2.2.9). The statistical significance of such data was further confirmed by the Kaplan-Meier estimation model, providing the evidence for the therapeutic effect of MCFG ($p < 0.05$) (Figure 2.2.10).

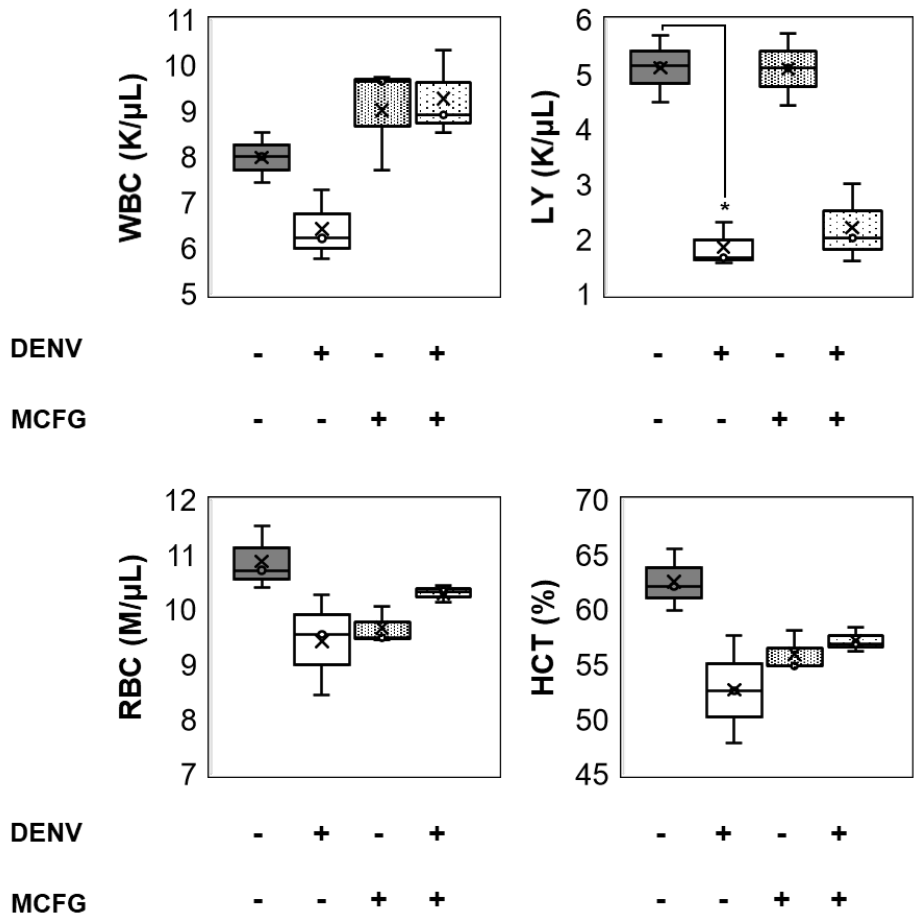

Figure 2.2.8 Hematology analysis table for each experimental group (n = 3). Experimental results are shown as a box-and-whisker plot. X in the box represents the average of each sample. Bars indicate MIN and MAX, from four individual groups. Neutrophil (NE), lymphocyte (LY), red blood cell (RBC), hematocrit (HCT), and * for $p < 0.05$.

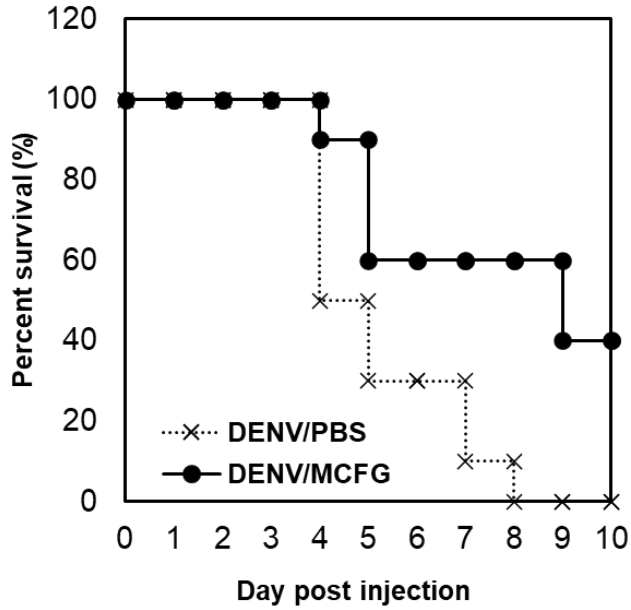

Figure 2.2.9 Survival rate of DENV-infected AG129 mice with or without MCFG treatment (n = 10).

MCFG given at a dose of 75 mg/kg i.p. once a day. Statistical significance was confirmed by a log-rank test ($p = 0.0046$).

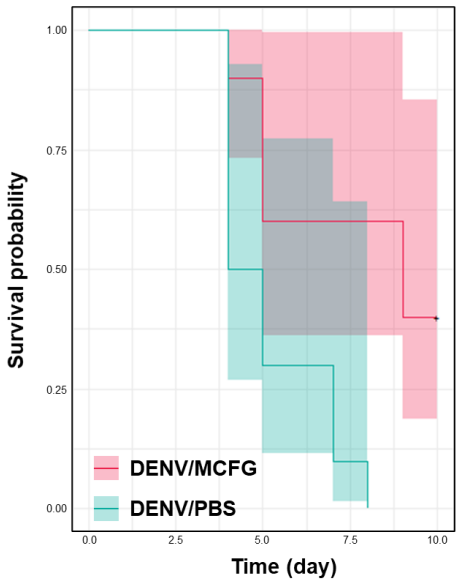

DENV/MCFG

Time (day)	Survival	Stderr	95% lower CI	95% upper CI
4	0.9	0.0949	0.732	1
5	0.6	0.1549	0.3617	0.9952
9	0.4	0.1549	0.1872	0.8545

DENV/PBS

Time (day)	Survival	Stderr	95% lower CI	95% upper CI
4	0.5	0.1581	0.269	0.9293
5	0.3	0.1449	0.1164	0.7732
7	0.1	0.0949	0.0156	0.642
8	0	NA	NA	NA

Pearson's chi-squared test	Chisq	DF	P-value
1	8.0461	1	0.0046

Figure 2.2.10 Kaplan-Meier analysis for MCFG treatment. DENV infected AG129 mice were administered with either MCFG of PBS (n = 10).

Analysis of the MCFG group was represented by a red line with the highlight indicating the 95% confidence interval, whereas the PBS group in green. The life table shown on the right side provides the individual statistical analysis at each representative time point. Pearson's chi-squared test was executed to determine the significance of the survival model. Degree of freedom (DF) and the p-value were calculated by log-rank test

In this study, we developed an RNA helicase assay based on GO, which we refer to as RheGO, which consists of GO as a cost-effective and easily prepared quencher, RNA as a crucial substrate, and DENV helicase as an active target. These constituents make RheGO a cost-effective, simple, and highly reliable assay to quantitatively measure helicase activity levels via fluorescence observations. Moreover, we demonstrate that this GO-based helicase assay has not only applied value for a well-studied model helicase acting on a DNA substrate but also scalable application for a general RNA helicase through analysis of DENV helicase, showing activity specific to RNA substrates.

Although there have been studies of MBHA for DENV helicase using RNA substrates,[47] RheGO has several advantages such as high reliability and reproducibility, cost-effectiveness, and simplicity by just adding GO. Moreover, RheGO provides more possibilities for discovering inhibitors than HTS based on fragment analysis of helicase such as nucleic binding and ATPase assays. Thus, RheGO can be a more robust method to discover potent DAAs.

MCFG is an antifungal drug approved by the U.S. FDA in 2005 to treat candidiasis caused by a fungal infection. The chemical structure of MCFG features a cyclic hexapeptide core with a lipid sidechain. MCFG targets the 1,3-β-d-glucan synthase and inhibits the production of fungal cell walls, however, the underlaying mechanism remains unknown.[48] Recent reports have suggested MCFG as an antiviral agent against enterovirus 71 and chikungunya virus.[49,50] However, these reports only evaluated the antiviral activities at the cellular level and did not reveal the antiviral mechanisms against the viruses. In contrast, our study aimed to identify the inhibitor targeting the viral RNA helicase. Based on our results, we suggest that the antiviral mechanism of MCFG against DENV is attributed to its helicase-inhibition activity. To the best of our knowledge, our study is the first to illustrate the antiviral effect of MCFG in an animal model.

In vitro, MCFG could inhibit the proliferation of DENV in cells as shown using the focus-reduction assay, analysis of relative viral RNA expression levels, and immunostaining of DENV antigen. Furthermore, similar viral inhibitor effects were found in the human cell line Huh-7, implying that the antiviral activity of MCFG does not merely affect a model cell line.

As MCFG is an FDA-approved drug, detailed information from clinical trials is available on the drug label in the FDA database, including dosing, adverse effects,

and toxicity. However, there is no information regarding adverse effects in animals and thus it is difficult to interpret the unexpected results from the animal experiments in the present study. For example, the number of RBC declined in normal mice following MCFG treatment, although the difference was not statistically significant ($p = 0.314$). In humans, the drug label indicates that high dosing could induce hemolysis, which is supported by a clinical report.[51] Another recent report claimed that MCFG induces hemolysis by triggering cell shrinkage and cell membrane scrambling in human erythrocytes.[52] Although further investigations on the effects of MCFG to mouse blood are warranted, we suspect that this effect may be related to a similar mechanism as proposed in humans. We also observed spleen enlargement in the MCFG-treated mice; although the spleen expansion was only reduced by 0.5-fold compared with that of the DENV-infected group, it was significantly ($p < 0.05$) enlarged relative to that of untreated healthy mice. There are several potential explanations for MCFG-induced splenomegaly, including splenic congestion, hematologic malignancies, and viral infection; immune hyperplasia has also been shown to result in spleen swelling.[53-55] Considering that a previous report demonstrated the ability of MCFG to stimulate phagocytic cells and the immune response in mice,[56] we suspect that the immune-stimulation effect of MCFG is mainly responsible for the observed increase in spleen size.

Nevertheless, our *in vivo* results suggested that MCFG could be a potential treatment for DENV infection as a DAA. The rationale can be explained as follows: The significant reductions of viremia and viral load levels in the tissues of the MCFG treatment group support the contention that MCFG acts directly on DENV replication. Moreover, the viremia level can be a marker of symptom

severity. For instance, in patients suffering from severe disease manifestations such as dengue hemorrhagic fever or dengue shock syndrome, viremia levels are 10-fold higher than those in patients with moderate symptoms of infection.[57,58] Here, we found that MCFG diminished viremia by approximately 8-fold, suggesting that MCFG may ameliorate disease severity. Furthermore, we observed reductions of hematocrit (HCT) and RBC levels in infected mice, indicating hemorrhage.[41,51] Treatment of DENV-infected mice with MCFG recovered HCT and RBC levels by 54% and 40%, respectively. In addition, the levels of inflammatory cytokines associated with severe manifestations were significantly reduced in DENV-infected mice treated with MCFG.[40,59] Overall, these results indicate that MCFG can alleviate hemorrhage resulting from severe cases of dengue.

The potential of having a helicase inhibitor as an antiviral agent has been assessed using the HSV helicase-primase inhibitor, pritelivir, discovered using enzyme assay based HTS.[60,61] Pritelivir dose-dependently reduced the rates of genital HSV shedding and days with lesions in a phase II clinical trial.[62] Based on these results, developments of viral helicase inhibitors targeting other viruses including HCV and DENV have been accelerated.[60] However, inhibitor for DENV helicase has yet to be identified[7] Although the effect of MCFG *in vivo* showed a potential treatment strategy against dengue, further preclinical investigations are warranted prior to clinical trials. For example, the level of protection from DENV infection provided by MCFG in mice may be considered unsatisfactory. To improve survival-rate, using other animal models could be an option. Although the AG129 mouse is suitable as a dengue infection model since it shows disease symptoms similar to those in humans, this model may underestimate the therapeutic effects since it lacks an innate immune response.[63] Furthermore, the

serum half-life of MCFG is shorter in mice (6.13 h) than in humans (11.3 to 20 h).[64] Considering the unfavorable pharmacokinetics of MCFG in mice, optimizing the dosing volume and schedule may improve the protection rate.

2.3 Conclusion

In summary, we utilized RheGO to identify MCFG as a promising DAA, which showed inhibitory effect against DENV proliferation both *in vitro* and *in vivo* and eventually enhanced survival rates by up to 40% in a lethal mouse model. RheGO could be used for analysis of other RNA helicases from various RNA viruses, such as the yellow fever virus, west Nile virus, Zika virus, and SARS-CoV-2, enabling preemptive responses to viral infectious diseases through discovery of effective antiviral agents.

2.4 Materials and Methods

Cloning, expression, and purification of the helicase recombinant protein

The coding sequence of the NS3 helicase domain (161-618) from dengue virus serotype 2 (DENV2) was given from Julien Lescar's group at Nanyang Technological University. The DENV2 helicase sequence was fused to the coding sequence of the N-terminal 10 His-tagged superfolder GFP (sfGFP) and inserted into the pET vector. The expression plasmid was amplified in the E. coli strain JM109, and purified plasmids were transformed into BL21RIPL. When O.D. reached from 1.0 to 1.2, transformed cells were induced by adding IPTG with a final concentration of 1 mM then incubated at 18°C for overnight. Next day, the transformed cells were harvested and resuspended in the phosphate buffer with 500 mM NaCl. The resuspended cells were lysed by sonication. The supernatant was collected and the desired protein was primarily purified by Ni-NTA column. The eluted proteins were further purified using a HiLoad 16/600 Superdex 200 pg column (GE Healthcare, USA). The peak fractions were pooled and concentrated to approximately 1 mg/mL. The concentrated proteins were flash-frozen in liquid nitrogen and stored at −80°C prior to using in inhibitor screening assay.

Preparation and characterization of graphene oxide (GO)

Graphene oxide nanosheets were prepared according to the previously reported Hummers method with slight modifications. Briefly, 0.5 g of natural graphite (FP 99.95% pure, Graphit Kropfmühl AG, Hauzenber g, Germany), 0.5 g of $NaNO_3$ (Junsei, Tokyo, Japan), and 23 mL of H_2SO_4 (Samchun, Seoul, Korea) were mixed in a beaker with vigorous stirring in an ice bath. 3 g of $KMnO_4$ (Sigma-Aldrich, MO, USA) was slowly added to the mixture. Then, the mixed solution was transferred into 35°C water bath with vigorous stirring. After an hour, 40 mL of

distilled water was added to the mixed solution and stirred for 30 min at 90°C. Another 100 mL of distilled water was added and followed by the drop-wise addition of 3 mL of 30% H_2O_2 (Junsei, Tokyo, Japan). During this addition, the color of the solution changed from dark brown to yellow. The mixture was purified by filtration with a Büchner funnel and washed with distilled water until the filtrate was neutralized. The filtered cake was dried in a desiccator. The GO was exfoliated in distilled water by sonication until there were no visible particles in the suspension.

An atomic force microscopy image and a height profile of the prepared GO were taken with an NX-10 (Park System, Korea). The Raman spectra of graphite and the prepared GO were obtained with LabRAM HR UV/vis/NIR (Horiba Jobin Yvon, France) using an Ar ion CW laser (514.5 nm) as the excitation source focused through a BXFM confocal microscope equipped with an objective (50X, numerical aperture=0.50). The FTIR spectrum of GO was obtained with an EQUINOX55 (Bruker, Germany) using the KBr pellet method.

In vitro helicase assay by gel-shift

To prepare the DENV2 helicase substrate, a mixture of each strand of DNA was prepared by the addition of 2 μL of 100 μM 3' TAMRA labeled DNA strand (5'-TTT AAG CAC CGT AAA GAC GC-3', Genotech, Daejeon, Korea) to a 2-fold excess of complementary RNA strand (5'-GCG UCU UUA CGG UGC UUA AAA CAA AAC AAA ACA AAA CAA AA-3', Bioneer, Daejeon, Korea) in an annealing buffer solution (10 mM Tris-HCl, pH 8.0 (Duchefa, Haarlem, Netherlands), 100 mM NaCl (Duchefa, Haarlem, Netherlands) and 1 mM EDTA (Duchefa, Haarlem, Netherlands)) as final volume 20 μL. Next, annealing was carried out using a heat block at 95°C for 5 min, followed by slow cooling at room temperature over 30

min.

For in vitro helicase assay, 2 pmole of double-strand substrate and 1000 pmole of trap DNA(5'-TTT AAG CAC CGT AAA GAC GC-3', Genotech, Daejeon, Korea) were added into 1x reaction buffer (25 mM Tris-HCL, pH 8.0, 1.3 mM MgCl2 (Duchefa, Haarlem, Netherlands), 6.25 mM NaCl, 10% glycerol (Duchefa, Haarlem, Netherlands)) including 10 mM ATP (Roche, Switzerland, 10519979001). Then, Mix Helicase with various concentration (19.5 - 78 nM) into substrate mixed reaction buffer to make total volume 20 μL and incubate at 37°C for 60 min.

Each sample was transferred to 15% native polyacrylamide gel and electrophoresis was performed at 100V for 15 min. Fluorescence of TAMRA from gels was analyzed by using Chemidoc (Bio-Rad, USA).

Complete blood count, viremia analysis, whole blood RNA expression analysis, and cytokine bead assay.

At day 3 post-infection (p.i.), blood was collected from each mouse and transferred into BD Microtainer tube with K2EDTA (BD, USA, 365974). After gentle mix by rocking for 10 min, 20 μL of each sample was analyzed for complete blood counts with HEMAVET 950FS (Drew Scientific, USA). The measured value of each factor was semi-quantitatively analyzed against that of the uninfected control. For analysis of viremia and expression change in cytokines, plasma was separated by centrifugation at 8000 g, 4°C for 15 min. Viremia and viral RNA expression in whole blood was analyzed by real-time PCR (Applied Biosystems, USA). To examine change in the expression of inflammatory cytokines, BD Cytometric Bead Array (BD, USA, 552364) was performed. All samples were analyzed according to the manufacturer's instruction.

GO based helicase assay

Prepare the annealed DENV2 helicase substrate as mentioned above. Then, a solution of helicase substrate was prepared by mixing 1 μL annealed substrate stock in 75 μL 1x reaction buffer (25 mM Tris-HCl, pH 8.0,1.3 mM $MgCl_2$, 6.25 mM NaCl, 10% glycerol).

GO solution was prepared at 2.5 μg/mL in a ATP solution (40 mM ATP, 25 mM Tris-HCl, pH 8.0, 1.3 mM $MgCl_2$, 6.25 mM NaCl, 10% glycerol) right before use from a 1 mg/mL GO solution in distilled water. To perform GO based helicase assay, 15 μL of the substrate solution and 15 μL DENV2 helicase were mixed in 96 well plates. Then, 30 μL of ATP-GO solution were added to the above mixture in the 96 well plates. The final concentrations of nucleic acid substrate, ATP, GO, DENV2 helicase were 33 nM, 20 mM, 1.25 μg/mL and 0-26 nM, respectively, in a total volume of 60 μL with 1x reaction buffer. Next unwinding activity of the helicase was measured over time at 37°C by monitoring fluorescence intensities at Ex/Em = 550 nm/570 nm (for TAMRA, substrate) with a fluorometer, SynergyMx (BioTek, UK).

Unwinding inhibition assay by graphene-oxide based platform

For AMP-PNP(Sigma-Aldrich, MO, USA) inhibition assay, 132 nM annealed substrate, and AMP-PNPs with various concentrations were mixed in 1x reaction buffer. 15 μL of substrate containing solution and 15 μL of helicase solution were mixed by equal amount, followed by addition of 30 μL of ATP-GO solution (40 mM ATP and 2.5 μg/mL GO in 1x reaction buffer). The final concentration of helicase was 26 nM. Fluorescence intensity measurement was performed by a fluorometer at at Ex/Em = 550 nm/570 nm after 60 min incubation at 37°C.

Measurement of the Z′-factor

For the positive control, 15 µL of 104 nM DENV2 helicases and 15 µL of 132 nM substrate solution were mixed in 96 well plates, followed by transfer of 30 µL of ATP-GO solution (40 mM ATP, 2.5 µg/ml GO in 1x reaction buffer). For the negative control, 15 µL of 104 nM boiled inactive (102°C for 5min) helicases and 15 µL of 132 nM substrate solution were mixed in 96 well plates, followed by transfer of 30 µL of ATP-GO solution. All plates were incubated for 60 min at 37°C. The fluorescence intensities were measured (Ex/Em = 550 nm/ 570 nm for TAMRA) (n=15). The Z′ -factor was calculated using below equation.

$$Z' = 1 - \frac{(3\sigma_{c+} + 3\sigma_{c-})}{|\mu_{c+} - \mu_{c-}|}$$

σ_{c+} : standard deviation of the positive control

σ_{c-} : standard deviation of the negative control

μ_{c+} : average of the positive control

μ_{c-} : average of the negative control

Screening of the drug library

Basically, screening was performed by applying the same condition for GO based helicase assay as described above except for addition of chemical library. 1,443 compounds from the FDA-approved Drug Library (Selleckchem, Houston, TX, USA) were first mixed with the helicase solution at 100 µM before the addition of a mixture of ATP-GO solution and double-strand nucleic acid substrates. After the addition of the mixture of helicases and library compounds to the mixture of the substrate and ATP-GO solution, the helicase activities for double-strand nucleic acid unwinding were evaluated by measuring the fluorescence intensity at Ex/Em=

550 nm / 570 nm for TAMRA after 60 min of incubation at 37°C using a fluorometer.

From the primary result of screening, counter screening was executed. The experimental condition of counter screening is same with screening procedure except that single-strand substrates were added instead of double-strand substrate.

Determination of the IC_{50}

Mixture of helicase and inhibitor compounds were prepared by mixing with a solution of 15 μL of 104 nM helicase and 0.4–4000 μM of the selected six hit compounds from chemical library. Then, 15 μL of substrate solution and 30 μL of ATP-GO solution were added into 96 well plates. Fluorescence intensities were measured at Ex/Em= 550 nm/570 nm (for TAMRA) after 60 min of incubation at 37°C. The IC_{50} values were determined by DoseRep sigmoidal curve-fit method with OriginPro 8 (OriginLab Corporation, Northampton, MA, USA).

Cell culture

Monkey kidney cell line (Vero E6) was kindly provided by Professor K. Ahn from Department of Biological Science, Seoul National University. Liver carcinoma cell line (Huh-7) was purchased from American Type Culture Collection Inc. (USA). Vero E6 and Huh-7 were maintained in Dulbecco's modified minimal essential medium (DMEM) (WelGENE Inc., Seoul, Korea, LM001-09) containing 4.5 g/L D-glucose supplemented with 10% fetal bovine serum (FBS) (WelGENE Inc., Seoul, Korea, LB204-01), 100 units/mL penicillin and 100 mg/mL streptomycin in 37°C temperature and 5% CO2 atmospheric condition unless otherwise stated.

CCK-8 assay for cell viability test

Vero E6 and Huh-7 cells were seeded in 96 well plates with 60–70% confluency (30,000 cells/well) and incubated for overnight. After the cells were treated with various concentration of the hit compounds for 48 h, the cells were washed with phosphate buffered saline (PBS, WelGENE, Korea) solution and incubated with 10 μL of Cell Counting Kit-8(CCK-8) (Dojindo Inc., Kumamoto, Japan, CK04) solution to analyze the active cells metabolically. CCK-8 treated cells were incubated for 1–4 h. Then, the absorbance was measured at 450 nm with a SynergyMx fluorometer.

Preparation of DENV2

DENV2(strain KBPV-VR-29) was obtained from Korea Bank for Pathogenic Viruses (Seoul, Korea). Virus stocks were amplified in Vero E6 cells. Briefly, Vero E6 cells were inoculated with viral inoculum for 2 h at 37°C(5 mL per T-75 flask) with shaking every 30 min, before addition of 15 mL medium with 2% FBS. Virus-inoculated cells were incubated at 37°C for 6-7 days before harvesting the supernatant. After harvest, the viruses were concentrated by ultracentrifugation (Optima L-100K with 70Ti- fixed angle rotor) at 36,000 rpm, 4°C for 3 h. All virus stocks were stored with 20% FBS at below -70°C before using.

Focus-forming unit (FFU) assay for viral titer determination

DENV2 titer was determined by infecting Vero E6 cells for 48 h with a 0.75% methylcellulose overlay and analyzing the plates for focus-forming units per mL (FFU/mL). To prepare 0.75% methylcellulose overlay, Mix 10 mL of 10xMEM (Thermo Fisher scientific, USA, 11430030), 1 mL of 100X GlutaMAX (Thermo Fisher scientific, USA, 35050061), 2.93 mL of 7.5% sodium bicarbonate (Thermo Fisher scientific, USA, 25080094), 1 mL of 100XP/S (WelGENE, Korea, LS202-

02), 2 mL of FBS (WelGENE, Korea), 33.07 mL of sterile D.W. and 50 mL of sterile 1.5% methylcellulose (Sigma-Aldrich, USA).

Briefly, cells were titrated with serially diluted virus in triplicates onto a monolayer culture of Vero E6 cells in 96 well plates and incubated at 37°C for 2 h. Virus inoculum was removed and replaced with a 0.75% methylcellulose overlay. Vero E6 cells were incubated for an additional 48 h before fixation with 4%PFA and incubated anti-flavivirus antigen, clone D1-4G2-4-15,(1:2000) (Merckmillipore, USA, MAB10216) overnight at 4°C. Then, cells were washed three times with PBS and incubated with FITC-conjugated anti-mouse secondary antibody (1:500) (Sigma-Aldrich, USA, F0257) for 1.5 h at room temperature. Cells were washed three times with PBS before DAPI staining.

Focus reduction assay for determination of EC_{50}.

Vero E6 cells were seeded in 96 well plates with 100% confluency. Cells were inoculated in triplicates with DENV2 (100 FFU/well) at 37°C for 2 h. Then, cells were incubated with a 0.75% methylcellulose overlay containing 0.1–1000 μM of hit compounds at 37°C for 2 days. After immuno-staining described above, The EC_{50} values were determined by DoseRep sigmoidal curve-fit method with OriginPro 8 (OriginLab Corporation, Northampton, MA, USA).

In vitro virus infection test

Before the experiment, Vero E6 and Huh-7 were seeded in densities of 20×10^4 cells/cm^2, respectively. After 24 hours of incubation under 5% CO2, 37°C, DENV2 was inoculated to each cell culture by multiplicity of infection of 0.1 and0.5, respectively, under serum-free culture media for 2 hours. The culture plates were gently rocked every 30 min for even distribution of the virus to the cells. Hit

compound solutions were prepared with a serially diluted concentration in each complete culture medium. After the incubation, virus medium was removed and the cells were washed with sterilized PBS once, followed by the treatment of the chemical solutions. The cells were incubated under the culture chamber for 48 h. After the incubation, the cells were prepared for the immuno-staining and relative viral RNA expression analysis. For immuno-staining, chemical solutions were removed and the cells were washed with sterilized PBS, followed by fixation with 4% paraformaldehyde. For viral RNA expression analysis, cells were treated with TRIzol after the washing process and stored at -70°C for further analysis.

Animal experiments

AG129 mice (129/Sv IFN-α/β, and -γ receptor deficient) were purchased from Marshall BioResources (UK). All experimental procedures were preapproved by IACUC of Seoul National University (Korea) and Jeonbuk National University (Korea) and were performed according to the guidelines of the recommendations from Association for Assessment and Accreditation of Laboratory Animal Care. As mosquitoes could transmit the DENV, the cages with filter cover were used to avoid any unexpected contact and contamination.

Mice infection and drug treatment

10 to 12 weeks-old mice were administered with 300 μL of virus stock including 1×10^7 FFU of DENV2 via the intraperitoneal (IP) route. For evaluation of antiviral efficacy of micafungin sodium (AvaChem, TX, USA, 2670S), DENV2 infected AG129 mice were administered 200 μL of micafungin sodium (75 mg/kg/day) by IP injection. Negative control (uninfected group) was administered with 300 μL PBS instead of the virus. For the drug control group, 200 μL of micafungin sodium

(75 mg/lg/day) was administered solely to the non-infected AG129 mice.

Survival rate analysis

The mortality state was monitored daily. In the survival analysis, euthanized mice exhibiting severe disease-associated symptoms were counted as the moribund state at the moment of the exhibition.

Mouse necropsy

At day 3 p.i., mice were sacrificed from each group (n = 5). Organ samples (spleen, liver, lung, small intestine, and large intestine) were collected and prepared for the virus RNA expression analysis and pathology analysis. Spleens were weighed to determine splenomegaly. For the virus RNA expression analysis, half of the spleen, liver and lung were homogenized and treated with TRIzol reagent and stored at blow -70°C for further analysis. The same procedures were applied to the whole samples of small intestine and large intestine. The other half of the spleen, liver, and lung were submerged to 4%PFA for fixation and stored at 4°C.

Relative viral RNA expression level analysis

For the investigation of viral RNA expression change in the collected specimens, RNA was isolated from each cell-based and animal-based sample treated with TRIzol (Invitrogen, USA, 15596018) and quantified by Take3 Micro-Volume Plate. Using 0.1–1 μg of total RNA, cDNA was synthesized by 5xRT-Master Mix with random hexamer (Elpisbiotech, Korea, EBT-1511) according to the instruction manual (reaction in a 20 μL volume at 42ºC for 60 min). For target gene amplification, each primer was designed in consideration of GC content less than 50%, overlapping between two exons of the target genes with the expected amplicon size of –100 bps and PCR efficiency from 90% to 110%. Primer

sequences were confirmed in table 2.4.1. Real-time PCR was conducted to quantify viral RNA. Each reaction was conducted in a 20 μL volume with 10–100 ng of cDNA and 0.2 μM of each primer by using POWER SYBR green PCR master mix (Applied Biosystems Inc., USA, 4367659). 7300 Real-Time PCR System and Quantstudio3 (Applied Biosystems Inc., USA) were utilized in this study in two-step amplification process (annealing/extension at 60ºC for 1 min and denaturation at 95ºC for 15 sec) with melting curve analysis. The result data were analyzed by each software (SDS v1.4.1 and The QuantStudio Design & Analysis Software v1.4.3). Threshold cycle (Ct) was automatically determined. Since NTC group showed Ct value over 36, we disposed of the result data over 36 Ct. For analysis of viremia, a linear correlative standard curve was established between log of the virus titer (FFU/ml) and the corresponding Ct value. A standard curve was derived against a serially diluted viral titer. The R^2 of standard curves was 0.9995–0.9997 and y-intercepts were determined as 39.089–43.676. PCR efficiency was 90–102% with a 3 log linear dynamic range. According to the equation of the standard curve, the virus in plasma was calculated. For cell-based groups and mice organ samples (including whole blood), relatively quantitative viral RNA was analyzed against that of the endogenous control, GAPDH.

Primer sequence information

Target	**Forward primer**	**Reverse primer**	**Access-ion #**	**size (bp)**
Human GAPDH	TCACTGCCACCCAGAAGACTG	GGATGACCTTGCCCACAGC	NM_002046	123
Mouse GAPDH	TGACCTCAACTACATGGTCTACA	CTTCCCATTCTCGGCCTTG	NC_000067	85
DENV NS1	GCTCCTTCAATG	CCTGAAACCCC	KP4068	65

	ACAATGCGCTG TA	TTCCACGAAAA GTC	04

Table 2.4.1 Primer sequences for the real-time PCR analysis

Pathology analysis

Organ samples fixed with 4%PFA went through series of procedures as follows: paraffin embedding, section, and stain with hematoxylin and eosin (H&E) at the pathology core facility in Center for Medical Innovation, Seoul National University Hospital (SNUH-CMI), Korea.

Statistical analysis

Data plots with concentration-dependent assays were analyzed using OriginPro 8 and GraphPad Prism 7. Briefly, logarithmic sigmoidal curves were fitted according to each dataset. Error bars indicate ± SEM unless stated otherwise. Statistical significance of the in vitro and in vivo antiviral efficacy analysis was evaluated by a two-tailed t-test. Statistical significance of the survival rate was analyzed by log-rank test with R (R Foundation for Statistical Computing, Austria).

2.5 References

1. Panghal, A.; Flora, S. J. S., In *Handbook on Biological Warfare Preparedness*, Flora, S. J. S.; Pachauri, V., Eds. Academic Press: 2020; pp 65-81.
2. Reperant, L. A.; Osterhaus, A., *Vaccine* **2017,** *35* (35 Pt A), 4470-4474.
3. Almaghaslah, D.; Kandasamy, G.; Almanasef, M.; Vasudevan, R.; Chandramohan, S., *Int J Clin Pract* **2020**, e13637.
4. Corbett, K. S.; Edwards, D. K.; Leist, S. R.; Abiona, O. M.; Boyoglu-Barnum, S.; Gillespie, R. A.; Himansu, S.; Schafer, A.; Ziwawo, C. T.; DiPiazza, A. T.; Dinnon, K. H.; Elbashir, S. M.; Shaw, C. A.; Woods, A.; Fritch, E. J.; Martinez, D. R.; Bock, K. W.; Minai, M.; Nagata, B. M.; Hutchinson, G. B.; Wu, K.; Henry, C.; Bahi, K.; Garcia-Dominguez, D.; Ma, L.; Renzi, I.; Kong, W. P.; Schmidt, S. D.; Wang, L.; Zhang, Y.; Phung, E.; Chang, L. A.; Loomis, R. J.; Altaras, N. E.; Narayanan, E.; Metkar, M.; Presnyak, V.; Liu, C.; Louder, M. K.; Shi, W.; Leung, K.; Yang, E. S.; West, A.; Gully, K. L.; Stevens, L. J.; Wang, N.; Wrapp, D.; Doria-Rose, N. A.; Stewart-Jones, G.; Bennett, H.; Alvarado, G. S.; Nason, M. C.; Ruckwardt, T. J.; McLellan, J. S.; Denison, M. R.; Chappell, J. D.; Moore, I. N.; Morabito, K. M.; Mascola, J. R.; Baric, R. S.; Carfi, A.; Graham, B. S., *Nature* **2020**, *586*, 567-571.
5. Rodriguez-Roche, R.; Gould, E. A., *Biomed Res Int* **2013,** *2013*, 690835.
6. Dighe, S. N.; Ekwudu, O.; Dua, K.; Chellappan, D. K.; Katavic, P. L.; Collet, T. A., *Eur J Med Chem* **2019,** *176*, 431-455.
7. Rajapakse, S.; Rodrigo, C.; Rajapakse, A., *Infect Drug Resist* **2012,** *5*, 103-

112.

8. Gan, V. C., *Curr Treat Options Infect Dis* **2014,** *6* (3), 208-226.

9. Lim, S. P., *Antiviral Res* **2019,** *163*, 156-178.

10. Low, J. G.; Gatsinga, R.; Vasudevan, S. G.; Sampath, A., *Adv Exp Med Biol* **2018,** *1062*, 319-332.

11. Ahammad, F.; Tengku Abd Rashid, T. R.; Mohamed, M.; Tanbin, S.; Ahmad Fuad, F. A., *Microorganisms* **2019,** *7*(9), 296; doi:10.3390/microorganisms7090296

12. Janai, H. K.; Marks, M. I.; Zaleska, M.; Stutman, H. R., *Pediatr Infect Dis J* **1990,** *9* (3), 209-211.

13. Durantel, D., *Curr Opin Invest Dr* **2009,** *10* (8), 860-870.

14. Yin, Z.; Chen, Y. L.; Schul, W.; Wang, Q. Y.; Gu, F.; Duraiswamy, J.; Kondreddi, R. R.; Niyomrattanakit, P.; Lakshminarayana, S. B.; Goh, A.; Xu, H. Y.; Liu, W.; Liu, B.; Lim, J. Y.; Ng, C. Y.; Qing, M.; Lim, C. C.; Yip, A.; Wang, G.; Chan, W. L.; Tan, H. P.; Lin, K.; Zhang, B.; Zou, G.; Bernard, K. A.; Garrett, C.; Beltz, K.; Dong, M.; Weaver, M.; He, H.; Pichota, A.; Dartois, V.; Keller, T. H.; Shi, P. Y., *Proc Natl Acad Sci U S A* **2009,** *106* (48), 20435-20439.

15. Hassany, S. M.; Hassan, W.; Abo-Alam, H.; Khalaf, M.; Nafeh, A. M.; Nasr-Eldin, E.; Mostafa, E. F., *Infect Drug Resist* **2020,** *13*, 1873-1880.

16. Low, J. G.; Ooi, E. E.; Vasudevan, S. G., *J Infect Dis* **2017,** *215* (suppl 2), S96-S102.

17. Kumar, R.; Harilal, S.; Gupta, S. V.; Jose, J.; Thomas Parambi, D. G.; Uddin, M. S.; Shah, M. A.; Mathew, B., *Eur J Med Chem* **2019,** *182*, 111602.

18. Mercorelli, B.; Palu, G.; Loregian, A., *Trends Microbiol* **2018,** *26* (10), 865-

876.

19. Oliveira, A. S. d.; Silva, M. L. d.; Oliveira, A. F. C. S.; Silva, C. C. d.; Teixeira, R. R.; De Paula, S. O., *Journal of the Brazilian Chemical Society* **2014**, *25*, 1759-1769.

20. Luo, D.; Vasudevan, S. G.; Lescar, J., *Antiviral Res* **2015,** *118*, 148-158.

21. Norazharuddin, H.; Lai, N. S., *Malays J Med Sci* **2018,** *25* (5), 6-15.

22. Mastrangelo, E.; Pezzullo, M.; De Burghgraeve, T.; Kaptein, S.; Pastorino, B.; Dallmeier, K.; de Lamballerie, X.; Neyts, J.; Hanson, A. M.; Frick, D. N.; Bolognesi, M.; Milani, M., *J Antimicrob Chemother* **2012,** *67* (8), 1884-1894.

23. Mukherjee, S.; Hanson, A. M.; Shadrick, W. R.; Ndjomou, J.; Sweeney, N. L.; Hernandez, J. J.; Bartczak, D.; Li, K.; Frankowski, K. J.; Heck, J. A.; Arnold, L. A.; Schoenen, F. J.; Frick, D. N., *Nucleic Acids Res* **2012,** *40* (17), 8607-8621.

24. Mukherjee, S.; Weiner, W. S.; Schroeder, C. E.; Simpson, D. S.; Hanson, A. M.; Sweeney, N. L.; Marvin, R. K.; Ndjomou, J.; Kolli, R.; Isailovic, D.; Schoenen, F. J.; Frick, D. N., *ACS Chem Biol* **2014,** *9* (10), 2393-2403.

25. Sweeney, N. L.; Hanson, A. M.; Mukherjee, S.; Ndjomou, J.; Geiss, B. J.; Steel, J. J.; Frankowski, K. J.; Li, K.; Schoenen, F. J.; Frick, D. N., *ACS Infect Dis* **2015,** *1* (3), 140-148.

26. Coutard, B.; Decroly, E.; Li, C.; Sharff, A.; Lescar, J.; Bricogne, G.; Barral, K., *Antiviral Res* **2014,** *106*, 61-70.

27. Borowski, P.; Niebuhr, A.; Mueller, O.; Bretner, M.; Felczak, K.; Kulikowski, T.; Schmitz, H., *J Virol* **2001,** *75* (7), 3220-3229.

28. Mukherjee, S.; Hanson, A. M.; Shadrick, W. R.; Ndjomou, J.; Sweeney, N. L.; Hernandez, J. J.; Bartczak, D.; Li, K.; Frankowski, K. J.; Heck, J. A.; Arnold, L. A.; Schoenen, F. J.; Frick, D. N., *Nucleic Acids Res* **2012,** *40* (17), 8607-8621.

29. Jang, H.; Kim, Y. K.; Kwon, H. M.; Yeo, W. S.; Kim, D. E.; Min, D. H., *Angew Chem Int Ed Engl* **2010,** *49* (33), 5703-5707.

30. Jang, H.; Ryoo, S. R.; Kim, Y. K.; Yoon, S.; Kim, H.; Han, S. W.; Choi, B. S.; Kim, D. E.; Min, D. H., *Angew Chem Int Ed Engl* **2013,** *52* (8), 2340-2344.

31. Dumont, S.; Cheng, W.; Serebrov, V.; Beran, R. K.; Tinoco, I., Jr.; Pyle, A. M.; Bustamante, C., *Nature* **2006,** *439* (7072), 105-108.

32. Frick, D. N., *Curr Issues Mol Biol* **2007,** *9* (1), 1-20.

33. Li, K.; Frankowski, K. J.; Belon, C. A.; Neuenswander, B.; Ndjomou, J.; Hanson, A. M.; Shanahan, M. A.; Schoenen, F. J.; Blagg, B. S.; Aube, J.; Frick, D. N., *J Med Chem* **2012,** *55* (7), 3319-3330.

34. Wang, C. C.; Huang, Z. S.; Chiang, P. L.; Chen, C. T.; Wu, H. N., *FEBS Lett* **2009,** *583* (4), 691-696.

35. Wu, J. H.; Bera, A. K.; Kuhn, R. J.; Smith, J. L., *Journal of Virology* **2005,** *79* (16), 10268-10277.

36. Lee, J.; Kim, J.; Kim, S.; Min, D. H., *Adv Drug Deliv Rev* **2016,** *105* (Pt B), 275-287.

37. Kim, J.; Park, S. J.; Min, D. H., *Anal Chem* **2017,** *89* (1), 232-248.

38. Hummers, W. S.; Offeman, R. E., *J Am Chem Soc* **1958,** *80* (6), 1339-1339.

39. Zhang, J. H.; Chung, T. D. Y.; Oldenburg, K. R., *J Biomol Screen* **1999,** *4* (2), 67-73.

40. Schul, W.; Liu, W.; Xu, H. Y.; Flamand, M.; Vasudevan, S. G., *J Infect Dis* **2007,** *195* (5), 665-674.

41. Tan, G. K.; Ng, J. K.; Trasti, S. L.; Schul, W.; Yip, G.; Alonso, S., *PLoS Negl Trop Dis* **2010,** *4* (4), e672.

42. Park, S. J.; Kim, J.; Kang, S.; Cha, H. J.; Shin, H.; Park, J.; Jang, Y. S.; Woo, J. S.; Won, C.; Min, D. H., *Sci Adv* **2020,** *6* (22), eaaz8201.

43. Sarathy, V. V.; White, M.; Li, L.; Gorder, S. R.; Pyles, R. B.; Campbell, G. A.; Milligan, G. N.; Bourne, N.; Barrett, A. D., *J Virol* **2015,** *89* (2), 1254-1266.

44. Barth, O. M.; Barreto, D. F.; Paes, M. V.; Takiya, C. M.; Pinhao, A. T.; Schatzmayr, H. G., *Mem Inst Oswaldo Cruz* **2006,** *101* (8), 905-915.

45. Barreto, D. F.; Takiya, C. M.; Schatzmayr, H. G.; Nogueira, R. M.; Farias-Filho Jda, C.; Barth, O. M., *Mem Inst Oswaldo Cruz* **2007,** *102* (2), 175-182.

46. Sarathy, V. V.; White, M.; Li, L.; Kaiser, J. A.; Campbell, G. A.; Milligan, G. N.; Bourne, N.; Barrett, A. D. T., *Sci Rep* **2018,** *8* (1), 4900.

47. Basavannacharya, C.; Vasudevan, S. G., *Biochem Biophys Res Commun* **2014,** *453* (3), 539-544.

48. Odds, F. C.; Brown, A. J. P.; Gow, N. A. R., *Trends in Microbiology* **2003,** *11* (6), 272-279.

49. Kim, C.; Kang, H.; Kim, D. E.; Song, J. H.; Choi, M.; Kang, M.; Lee, K.; Kim, H. S.; Shin, J. S.; Jeong, H.; Jung, S.; Han, S. B.; Kim, J. H.; Ko, H. J.; Lee, C. K.; Kim, M.; Cho, S., *Virol J* **2016,** *13*, 99.

50. Ho, Y. J.; Liu, F. C.; Yeh, C. T.; Yang, C. M.; Lin, C. C.; Lin, T. Y.; Hsieh, P. S.; Hu, M. K.; Gong, Z.; Lu, J. W., *Antiviral Res* **2018,** *159*, 134-

142.

51. Nanri, T.; Iwanaga, E.; Fujie, S.; Yamada, Y.; Horikawa, K.; Mitsuya, H.; Asou, N., *Int J Hematol* **2009,** *89* (2), 139-141.

52. Peter, T.; Bissinger, R.; Signoretto, E.; Mack, A. F.; Lang, F., *Cell Physiol Biochem* **2016,** *39* (2), 584-595.

53. Pozo, A. L.; Godfrey, E. M.; Bowles, K. M., *Blood Rev* **2009,** *23* (3), 105-111.

54. Bronte, V.; Pittet, M. J., *Immunity* **2013,** *39* (5), 806-818.

55. Chapman, J.; Bansal, P.; Goyal, A.; Azevedo, A. M., Splenomegaly. In *StatPearls*, Treasure Island (FL), 2020.

56. Fuchs, B. B.; Li, Y.; Li, D.; Johnston, T.; Hendricks, G.; Li, G.; Rajamuthiah, R.; Mylonakis, E., *Mycopathologia* **2016,** *181* (1-2), 17-25.

57. Vaughn, D. W.; Green, S.; Kalayanarooj, S.; Innis, B. L.; Nimmannitya, S.; Suntayakorn, S.; Endy, T. P.; Raengsakulrach, B.; Rothman, A. L.; Ennis, F. A.; Nisalak, A., *J Infect Dis* **2000,** *181* (1), 2-9.

58. Libraty, D. H.; Endy, T. P.; Houng, H. S.; Green, S.; Kalayanarooj, S.; Suntayakorn, S.; Chansiriwongs, W.; Vaughn, D. W.; Nisalak, A.; Ennis, F. A.; Rothman, A. L., *J Infect Dis* **2002,** *185* (9), 1213-1221.

59. Sehrawat, P.; Biswas, A.; Kumar, P.; Singla, P.; Wig, N.; Dar, L.; Sood, R., *Mediterr J Hematol I* **2018,** *10*, e2018023.

60. Kwong, A. D.; Rao, B. G.; Jeang, K. T., *Nat Rev Drug Discov* **2005,** *4* (10), 845-853.

61. Biswas, S.; Sukla, S.; Field, H. J., *Future Med Chem* **2014,** *6* (1), 45-55.

62. Wald, A.; Corey, L.; Timmler, B.; Magaret, A.; Warren, T.; Tyring, S.; Johnston, C.; Kriesel, J.; Fife, K.; Galitz, L.; Stoelben, S.;

Huang, M. L.; Selke, S.; Stobernack, H. P.; Ruebsamen-Schaeff, H.; Birkmann, A., *N Engl J Med* **2014,** *370* (3), 201-210.

63. Chen, Y. L.; Yin, Z.; Duraiswamy, J.; Schul, W.; Lim, C. C.; Liu, B.; Xu, H. Y.; Qing, M.; Yip, A.; Wang, G.; Chan, W. L.; Tan, H. P.; Lo, M.; Liung, S.; Kondreddi, R. R.; Rao, R.; Gu, H.; He, H.; Keller, T. H.; Shi, P. Y., *Antimicrob Agents Chemother* **2010,** *54* (7), 2932-2939

64. Gumbo, T.; Drusano, G. L.; Liu, W.; Kulawy, R. W.; Fregeau, C.; Hsu, V.; Louie, A., *Antimicrob Agents Chemother* **2007,** *51* (3), 968-974.

Chapter 3. Graphene Oxide-treated Surface of Pure Titanium Promotes Adhesion and Proliferation of Human Gingival Fibroblast

3.1 Introduction

With the increasing life expectancy of modern society, the preservation and maintenance of teeth has become challenging. Consequently, many people replace missing teeth, typically by using bridges and dentures. Surgical implantation is the most frequently performed method for replacing missing teeth as it creates sufficient primary stability by interlocking the implant material and bone trabeculae.[1]

Because implants are inserted into a biological environment, implant materials with excellent physicochemical properties must be used.[2] As a material that exhibits excellent biocompatibility and strong resistance to corrosion, pure titanium (Ti) meets this criterion; consequently, it is among the most commonly used materials in dental implants. Moreover, the biocompatibility of titanium can be controlled by modifying its surface texture. For example, when sandblasted, large-grit, acid-etching (SLA) method is performed, the surface roughness of titanium increases, which enhances the removal torque, bone-to-implant contact, and cell adhesion, resulting in superior implant material properties.[3]

Furthermore, osseointegration and soft tissue sealing are essential factors for implantation. A soft tissue seal that surrounds and connects soft tissue and the implant contributes to the success of the implant.[4, 5] If the soft tissue seal is weak, the implant can be easily loosened by external impact. Likewise, since titanium is bioinert, loosening occurs, which shortens the service life of the implant. Therefore,

various surface fabrication methods are being studied to increase the bioactivity of implant materials to strengthen soft tissue sealing.[6-8]

Among carbon nanomaterials, graphene oxide (GO), which is a graphene derivative with oxygen functional groups, has unique physicochemical properties and excellent biocompatibility. Therefore, it can be applied to biosensor platforms, drug delivery carriers, and tissue engineering materials.[9-11] Previously, we reported that a layer of GO could enhance cell adhesion and proliferation.[12] However, the response of human gingival fibroblasts (HGFs), which are cells that participate in soft tissue sealing, to GO has not been evaluated accurately yet.

Here, we analyzed the changes in the physicochemical properties of GO-coated implant material and evaluated its effect on the adhesion, spread, and proliferation of HGFs on the substrate surface. No change in physical properties such as the roughness of the implant material surface was observed after GO coating. Moreover, the improvement in cell adhesion and proliferation was confirmed by evaluating the cellular interaction with GO, which initially promoted the expression of the cell adhesion genes in HGFs.

3.2 Results

Preparation and analysis of GO-coated substrates

In this study, we synthesized GO based on a previously reported method.[13] The GO sheets with single-layered structures were examined using atomic force microscopy (AFM) (Figure 3.2.1A). Through Fourier-transform infrared spectroscopy (FT-IR), the stretching peaks of oxygen functional groups such as C–O and C=O were confirmed at 1051 cm^{-1} and 1718 cm^{-1}, respectively (Figure 3.2.1B). Raman spectroscopy revealed a D peak indicating a structural disorder and a G peak that was attributed to the sp^2 domain at 1370 cm^{-1} and 1591 cm^{-1}, respectively (Figure 3.2.1C).

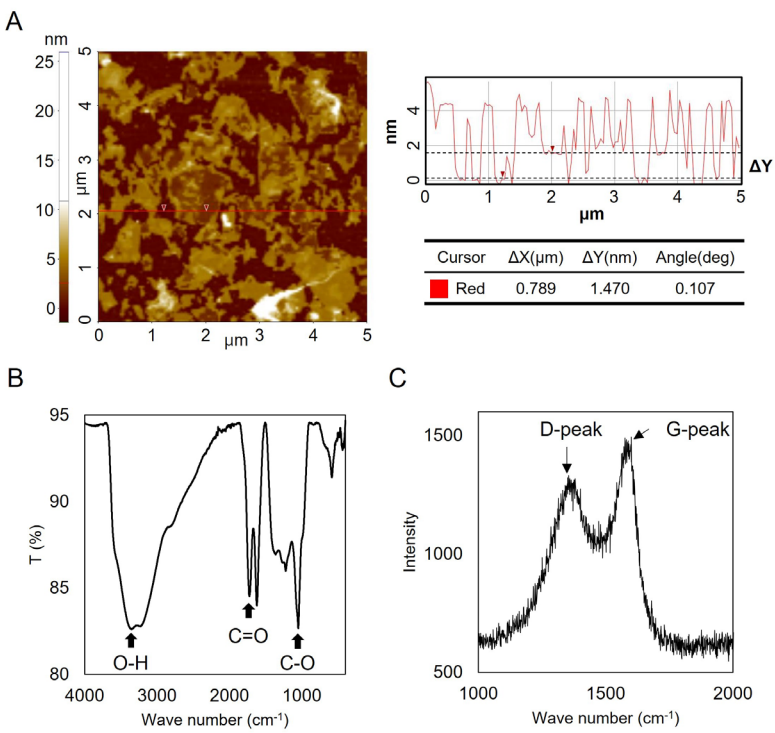

Figure 3.2.1 Characterization of graphene oxide (GO).

(A) The height profile and morphology of GO examined by AFM. (B) Oxygen functional groups of GO are confirmed by FT-IR. (C) GO specific Raman peaks, D- and G-peak, are determined.

Then, Ti and SLA discs were chemically modified to form a positively charged metal surface through silanization and then coated with GO via electrostatic interaction. After sample preparation, we first investigated the change in surface morphologies for all discs (Figure 3.2.2). In the Ti discs, a flat surface with scratches resulting from polishing was observed. Unlike Ti discs, the surface of the SLA discs became rough and irregular and small holes were formed. After the immobilization of GO, no significant morphological changes were observed on the Ti and SLA discs, even at high magnification.

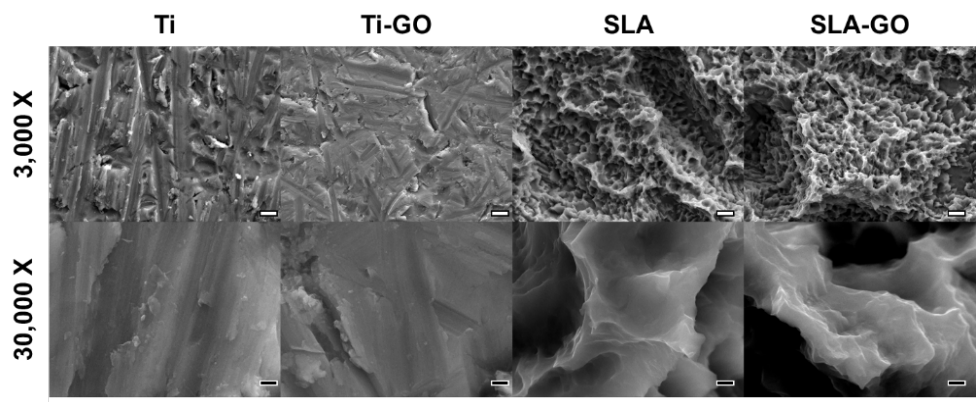

Figure 3.2.2 Scanning electron microscopy (SEM) images of Ti, Ti-GO, SLA, and SLA-GO discs.

The white and black scale bars represent 3 μm and 300 nm, respectively.

Next, we examined the surface roughness of all substrates by confocal laser scanning microscopy (CLSM) (Figure 3.2.3). As shown in the SEM image, all roughness parameters increased in the SLA discs compared to the Ti discs. After GO coating, all surface roughness parameters were slightly reduced, but no statistically significant differences were found (Table 3.2.1).

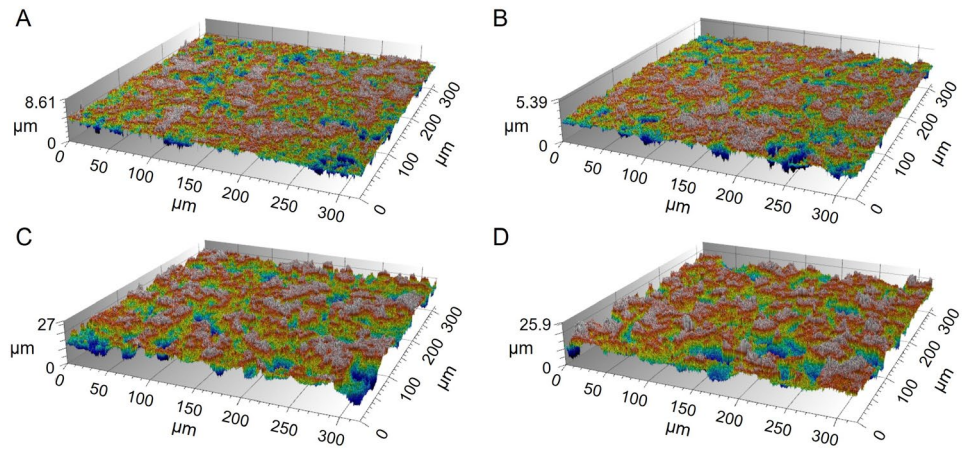

Figure 3.2.3 3D view of the surface of (A) Ti, (B) Ti-GO, (C) SLA, and (D) SLA-GO discs by CLSM

	Ti	Ti-GO	SLA	SLA-GO
Ra (μm)	0.25±0.01	0.22±0.03	2.00±0.45	1.73±0.38
Rq (μm)	0.32±0.02	0.29±0.02	2.49±0.55	2.19±0.40
Rv (μm)	1.03±0.19	0.88±0.16	5.92±1.35	5.72±0.15
Rp (μm)	0.92±0.19	0.86±0.13	5.21±0.44	4.89±1.15
Rc (μm)	0.75±0.14	0.64±0.08	4.13±0.40	4.06±0.97

Table 3.2.1 Surface roughness parameters of each substrate

To confirm the existence of GO on the surfaces of both Ti and SLA discs, the samples were analyzed using Raman spectroscopy, energy dispersive X-ray spectroscopy (EDS), and X-ray photoelectron spectroscopy (XPS). First, Raman spectra analysis showed the coexistence of D and G bands in GO-coated discs but not in non-coated discs (Figure 3.2.4). Although the Ti peak occupies a high proportion in all samples in the EDS analysis, the atomic percentages of carbon and

oxygen increased by approximately 1.9- and 1.3-fold, respectively, for both GO-coated Ti and SLA substrates (Figure 3.2.5).

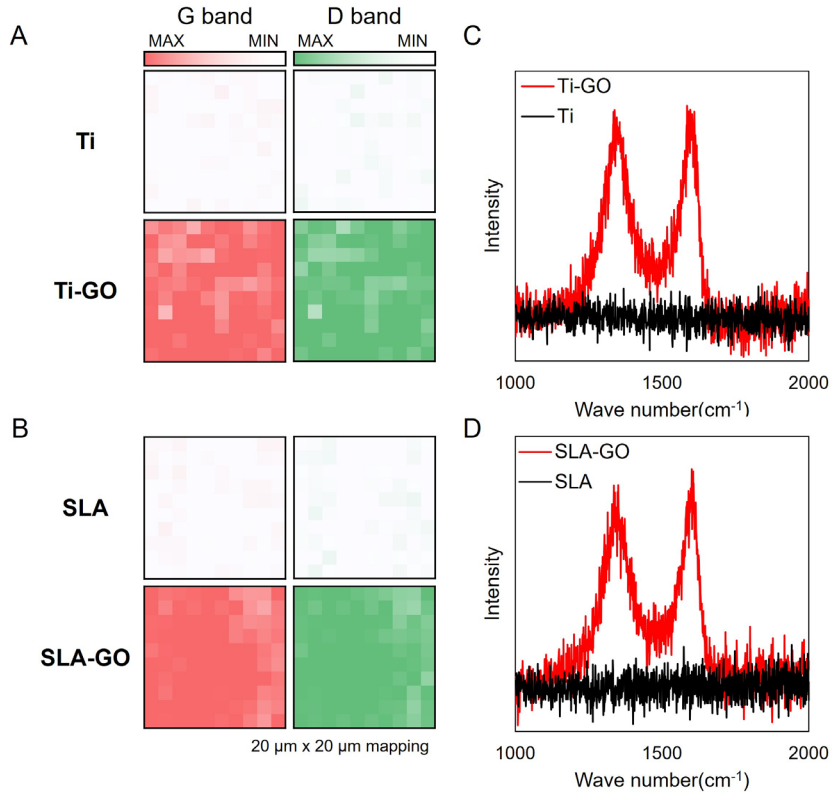

Figure 3.2.4 Raman mapping analysis (20 μm × 20 μm) of each substrate.
(A) Ti and Ti-GO. (B) SLA and SLA-GO. Red and green represent the intensity of G band (1600 cm^{-1}) and D band (1350 cm^{-1}), respectively. (C, D) Representative Raman spectra of each substrate.

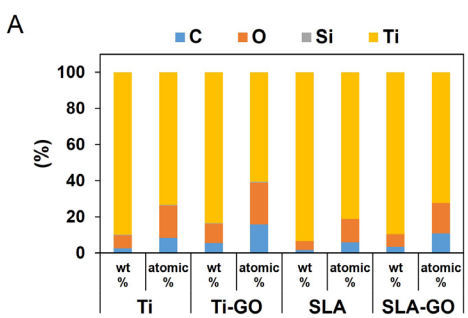

B

		C	O	Si	Ti
Ti	wt %	2.55	7.32	0.25	89.87
	atomic %	8.31	17.91	0.35	73.42
Ti-GO	wt %	5.45	10.59	0.48	83.48
	atomic %	15.79	23.01	0.6	60.6
SLA	wt %	1.66	5.01	0	93.33
	atomic %	5.76	13.05	0	81.18
SLA-GO	wt %	3.32	7.03	0	89.64
	atomic %	10.69	16.99	0	72.32

Figure 3.2.5 (A) Stacked column chart of EDS analysis for each substrate. (B)

Weight (wt) and atomic percentage of each element.

The XPS survey spectra of all samples measured in the energy range of 1200–0 eV are shown in Figure 3.2.6. In the spectra of all samples, the typical Ti 2s, Ti 2p, O 1s, and C 1s signals for the native TiO_2 film were detected. The chemical states of carbon were analyzed to compare the non-coated discs with the GO-coated discs. GO-coated discs showed stronger oxidized carbon states, including C–O, C=O, and C(O)O peaks, than non-coated discs (Figure 3.2.7).

Therefore, we determined that GO is present on the surface of the disc after immobilization of GO, and the GO coating did not change the surface morphology or roughness.

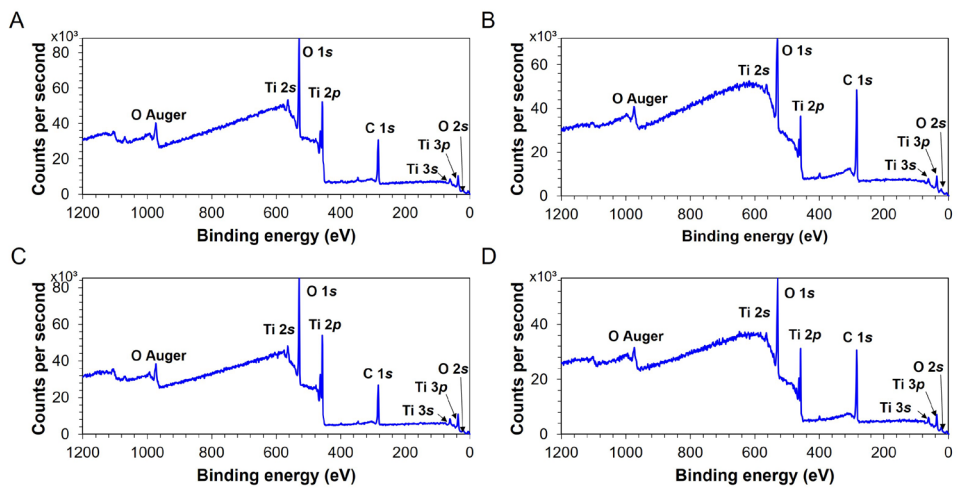

Figure 3.2.6 XPS survey spectra of (A) Ti, (B) Ti-GO, (C) SLA, and (D) SLA-GO discs

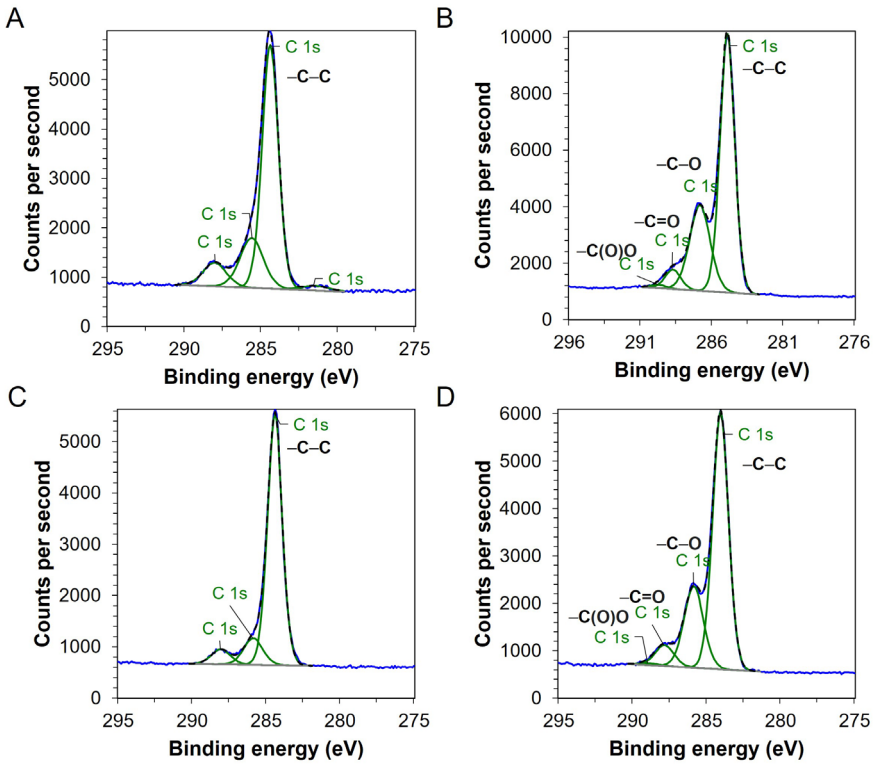

Figure 3.2.7 The chemical states of C 1s in (A) Ti, (B) Ti-GO, (C) SLA, and (D) SLA-GO discs

GO coating enhances cell attachment and cell proliferation

The early stage of cell adhesion considerably affects subsequent cell behaviors, including cell growth and proliferation. Therefore, we first investigated the initial stages of cell adhesion.[12]

HGFs were seeded at a density of 10×10^4 cells on each substrate and cultured sequentially for 0.5, 1, and 2 h. After paraformaldehyde fixation and staining with DAPI, the number of attached cells per unit area was counted (Figure 3.2.8). The cell number showed the following trend at all time points: SLA-GO > SLA > Ti-GO > Ti. The results of the analysis of variance (ANOVA) with *post hoc* Tukey test confirmed that significantly more cells adhered to the surfaces of Ti-GO, SLA, and SLA-GO discs than the Ti disc. In addition, we examined the effect of the GO coating on both Ti and SLA substrates. At 0.5 h, the number of cells on Ti and SLA substrates increased by 111.4% and 106.5%, respectively. In addition, at 1 h, it increased by 119.3% and 107.6%, respectively, on the GO-coated discs. We found that these trends were statistically significant using the t-test. Although the number of attached cells increased by 107.5% and 102.2% at 2 h, the SLA group did not show statistical significance ($p = 0.386$). Thus, the results suggests that GO might enhance the early stage of cell adhesion on both Ti and SLA substrate.

The CCK-8 assay was performed to evaluate the cell proliferation on different substrates. As shown in Figure 3.2.9, the number of cells increased in a time-dependent manner (Figure 3.2.9A). After Day 1, although a slight but statistically significant increase between the Ti and SLA groups was observed (ANOVA, $p < 0.0001$), there was no significant difference in the cell proliferation on both the Ti and SLA discs ($p = 0.03$ and $p = 0.21$). However, it was confirmed that the number of cells on GO-coated Ti and SLA substrates increased by 122.4% and 110.7%,

respectively, on day 4, suggesting that GO coating had a greater effect on cell proliferation than the SLA surface did in the early stage of cell growth.

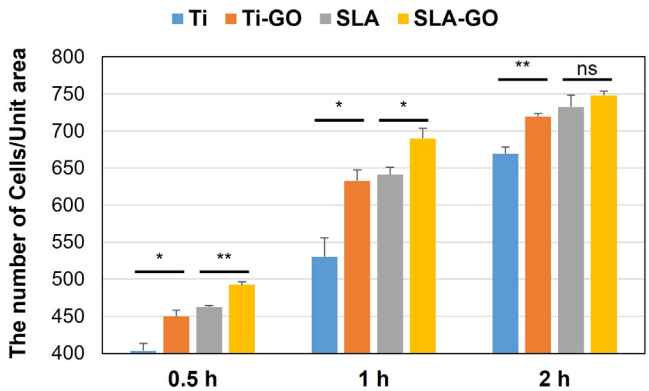

Figure 3.2.8 The number of attached cells on all substrates.
Bars in the graph indicate the standard error of mean (±SEM). *p < 0.05, **p < 0.005.

After day 7, the SLA group showed enhanced proliferation compared to the Ti group. In addition, GO-coating affected cell proliferation the most, showing a 124.5% and 112.7% increase in absorbance in the Ti and SLA substrates, respectively, on day 7. After day 10, the difference in the proliferation affected by GO-coating was reduced and was not observed on day 14. Moreover, we found that the number of cells in the SLA group was higher than that in the Ti group. This suggests that the SLA group can accommodate more cells than the Ti group.

Furthermore, to compare the cell proliferation rates on each substrate, the cell growth curves are shown in Figure 3.2.9B. This result indicates that the SLA group accelerated the proliferation rate of HGFs compared to the Ti group. In addition, by comparing the slopes of the growth curves between Day 4 and 7, it was found that the GO coating significantly affected the cell proliferation rate in the Ti and SLA groups.

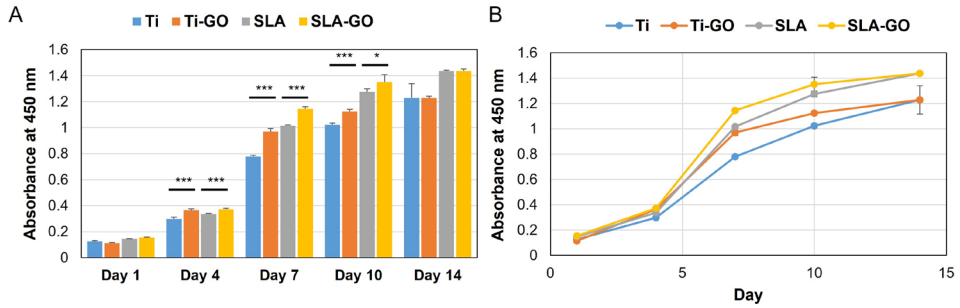

Figure 3.2.9 The proliferation of HGFs on different substrates.

(A) Bar graph. *p < 0.05, ***p < 0.0005. (B) Growth curves of HGFs for each substrate. Bars in the graph indicate the ±SEM.

The expression levels of adhesion-associated genes such as integrin β-1 (ITGB1), talin (TAL), focal adhesion kinase (FAK), and vinculin (VCL) were analyzed using real-time PCR to investigate the differences in gene expression (Figure 3.2.10).[12] When Ti and SLA substrates were coated with GO, the expression levels of TAL, FAK, and VCL were slightly higher than those on non-coated substrates at 0.5 and 1 h. The differences in the gene expression levels between the GO-coated and non-coated substrates diminished over time. However, it was not possible to confirm the specific pattern of changes in the expression of ITGB1 in each sample over the entire period. These results suggest that GO could promote the initial expression of focal adhesion-associated genes such as TAL, FAK, and VCL on both substrates and maintain the increased expression levels.

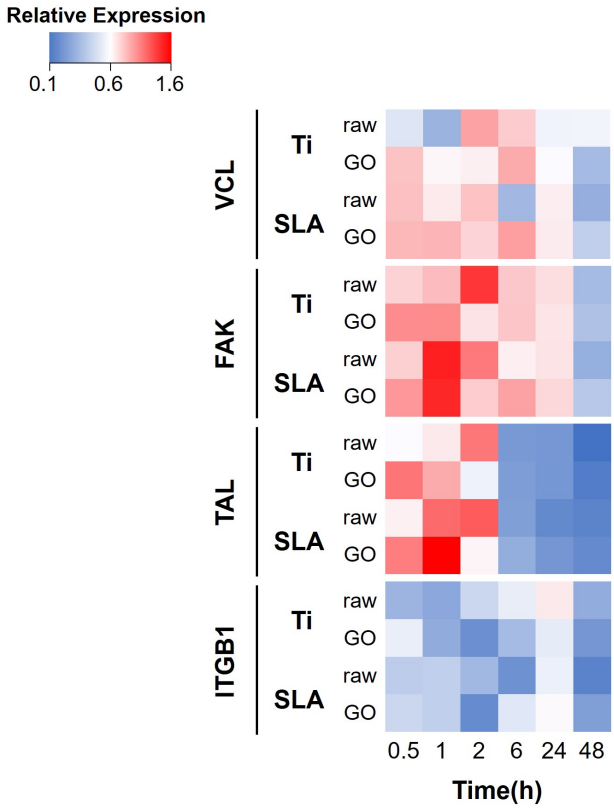

Figure 3.2.10 The expression patterns of focal adhesion-associated genes on different substrates.

ITGB1: integrin β-1, TAL: talin, FAK: focal adhesion kinase, and VCL: vinculin

In addition, we investigated the effect of GO coating on the cell morphology. Microscopic observation revealed significant differences in cell morphology between the Ti and SLA groups. However, there was no change in the GO-coated groups (Figure 3.2.11A). Furthermore, to quantitatively compare the cell morphology of cells on each substrate, round shape indexes (RSI) were calculated as the ratio between the areas of the cell and circumcircle (Figure 3.2.11B). As the RSI value approaches 0, the morphology of the cell becomes more linear, and as the value reaches 1, it becomes circular. In both the Ti and Ti-GO groups, the average RSI values were 0.451 and 0.466, respectively. The data showed no

statistically significant difference between the two groups. In addition, the average RSI values of SLA and SLA-GO (0.235 and 0.215, respectively) did not show a statistically significant difference. Overall, GO coating did not exhibit any notable effect on cell morphology.

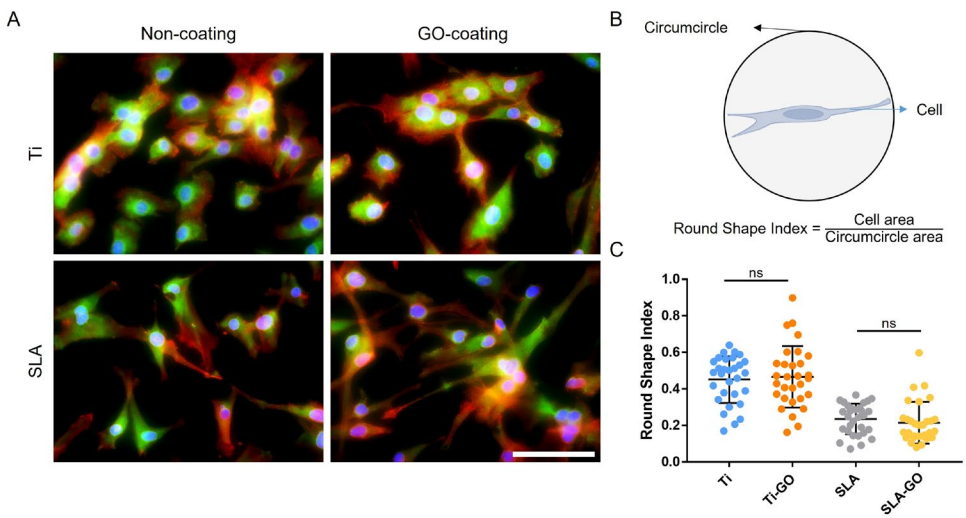

Figure 3.2.11 Morphological analysis of HGFs on each substrate (24 h).
(A) The images of the cell morphologies depict the nucleus (blue), vinculin (green), and actin (red). Scale bar represents 200 μm. (B) Equation for calculating round shape index. (C) Dot plot graph depicting the round shape index of cells on each substrate (n = 30). The longest middle lines of the graph represent the average of each sample. Bars in the graph indicate the ±SEM

In this study, we found that GO coating elicited different responses from HGFs to the implant material. In particular, HGF attachment and proliferation were enhanced on GO-coated substrates. Thus, we can speculate an explanation based on the following.

According to previous reports, GO could provide the possibility of non-covalent interactions, including electrostatic interactions, hydrogen bonding, and π-π

stacking due to its oxygen functional groups and aromatic domains.[14] Thus, GO can adsorb small molecules and proteins such as hormones and growth factors on its surface. For example, a report has shown that proteins and other biomolecules adsorbed on GO induce differentiation of stem cells.[15] Another report showed that GO increases integrin-mediated cell adhesion due to the adsorption of fibronectin on GO by interacting with its oxygen functional groups.[16] Therefore, we suggest that GO could enhance the HGF proliferation by increasing the local concentration of cellular factors such as serum proteins, fibroblast growth factor, insulin, and hydrocortisone, which induce HGF growth. In addition, it can be inferred that enhanced cell adhesion might have occurred due to the interaction between GO and fibronectin, which increases the chance of integrin interaction on the cell membrane.

Based on another report, an increase in surface roughness leads to an increase in the surface area, which allows the adsorption of various proteins, which, in turn, increases cell adhesion.[17] In this study, the difference in cell adhesion due to the change in surface roughness was confirmed with and without SLA. However, there was no significant difference in surface roughness based on the presence of GO coating. Therefore, we believe that the change in the nanoscale roughness induced by GO had a negligible effect on the micro-scale roughness.

3.3 Conclusion

In summary, we found that the adhesion and proliferation of HGFs, which contribute to soft tissue sealing, was increased owing to the enhanced expression of focal adhesion proteins on GO-coated Ti substrates. Therefore, based on the results of this study, we believe that GO coating material can be applied to implants as well as tissue engineering as it enhances pertinent cellular behaviors such as adhesion and proliferation.

3.4 Materials and Methods

Preparation of specimens

With commercially pure grade IV titatinum (Ti), Ti discs (diameter: 20 mm, thickness: 0.5 mm) were fabricated for this study. Manufactured samples (discs) were screened for any defects, then divided into 4 groups for further surface treatment. Two by two factorial design was carried out to evaluate the effect of two surface modification procedures: graphene oxide (GO) treatment and sandblasted, large-grit, acid-etched (SLA) treatment. For SLA treated groups, Ti surfaces were first sandblasted with large alumina (Al_2O_3) particles (50 μm in size, 4.5 x 105 Pa in blasting pressure). Then, the samples were etched in hydrochloric acid solution, rinsed, and dried for processing. Graphene oxide treatment procedure will be further described in details below.

Negative control group was turned Ti group without any surface modification: (GO - , SLA -). Positive control group was SLA treated Ti group with no GO application (GO - , SLA +). The in vitro study was conducted using Ti discs.

GO synthesis

Graphene oxide nanosheets were synthesized with minor modifications according to the previously reported Hummers method. At first, 0.5 g of natural graphite (FP 99.95% pure, Graphit Kropfmühl AG, Hauzenber g, Germany), 0.5 g of $NaNO_3$ (Junsei, Tokyo, Japan), and 23 mL of H_2SO_4 (Samchun, Seoul, Korea) were mixed in a beaker with vigorous stirring in an ice bath. 3 g of $KMnO_4$ (Sigma-Aldrich, MO, USA) was slowly added to the mixture and the mixed solution was transferred into a 35°C water bath with vigorous stirring for an hour. after adding 40 mL of distilled water to the mixed solution, the mixture was stirred for 30 min at 90°C.

Then, another 100 mL of distilled water was poured and followed by the drop-wise addition of 3 mL of 30% H_2O_2 (Junsei, Tokyo, Japan). During this addition, the color of the solution changed from dark brown to yellow. After the color change is finished, the reaction mixture was filtered with a Büchner funnel and washed with distilled water until the filtrate was neutralized. The filtered cake was dried and redispersed in distilled water by sonication until there were no visible particles in the suspension.

An atomic force microscopy image and a height profile of the prepared GO were taken with an NX-10 (Park System, Korea). The Raman spectra of GO was obtained (inVia Raman Microscope, RENISHAW, U.K.) by using an Ar ion CW laser (514.5 nm) as the excitation source focused through a confocal microscope equipped with an objective (20X, numerical aperture=0.50). The FTIR spectrum of GO was obtained with an EQUINOX55 (Bruker, Germany) using the KBr pellet method.

Preparation of GO-coated specimens

First, all specimens are cleaned 3 times by ultrasonication for 15 min with alternating water and ethanol. Then, the cleaned substrates were immersed in 10 mM anhydrous toluene solution of 3-APTES for 30 min, briefly sonicated in toluene, washed with ethanol and water, dried by blowing nitrogen gas. Graphene oxide sheets were immobilized on the 3-APTES-treated substrate via electrostatic interaction by immersing the substrates in graphene oxide aqueous suspension (0.5 mg/mL) for 1 h, washed with water and ethanol, and dried by blowing nitrogen gas.

Surface characteristics

The Raman spectra of GO from GO coated samples were obtained (inVia Raman

Microscope, RENISHAW, U.K.) by using an Ar ion CW laser (514.5 nm) as the excitation source focused through a confocal microscope equipped with an objective (20X, numerical aperture=0.50). Surface morphologies of various samples were observed by a field-emission scanning electron microscope (JSM-7800F Prime, JEOL Ltd, Japan) with an accelerated voltage of 15 kV. For elementary analysis of the samples, the Energy-Dispersive Spectroscopy (EDS) was performed (JSM-7800F Prime, JEOL Ltd, Japan). The chemical state of all samples were detected by X-ray photoelectron spectroscopy (AXIS SUPRA, Kratos, U.K) with an monochromatic Al(1486.7 eV) source. The surface roughness of each sample was measured by confocal laser scanning microscope (LSM800, Carl Zeiss, Germarny)

Cell culture

Human Gingival Fibroblast (HGF) was purchased from American Type Culture Collection Inc.(ATCC) (USA, PCS-201-018). HGF was maintained in Fibroblast Basal Medium (ATCC, USA,PCS-201-030) supplemented with the growth kit (ATCC, USA, PCS-201-041) which containing 5 ng/mL rhFGF b, 7.5 mM L-gultamine, 50 ug/mL ascorbic acid, 1 ug/mL hydrocortisone hemisuccinate, 5 ug/mL rh Insulin, 2% fetal bovine serum; 10 units/mL penicillin, 10 ug/mL streptomycin, and 25 ng/mL amphotericin B (MERCK, Germany, A5955) in 37°C temperature and 5% CO2 atmospheric condition unless otherwise stated.

Cell adhesion

For investigating the cell adhesion on each substrate, HGFs were seeded in 12-well plates at a density of 10×10^4 cells per well and cultured for 0.5, 1, and 2 h. At each time point, the samples were washed with PBS and fixed for at least 10 min

by using 4% paraformaldehyde (PFA) Then, HGF were rinsed with PBS and treated with DAPI (1 ug/mL). The fluorescence images of adhered cells on the substrates were taken with an inverted fluorescence microscope (IX71, Olympus, Japan) equipped with a CoolSNAPcf charge-coupled device (CCD) camera (Photometrics, Tuscon, USA).

Cell proliferation

HGFs were seeded in 12-well plates at with 1×10^4 cells/well and cultured for 1, 4, 7, 10, and 14 d. At each time point, the cells were treated with 100 μL of Cell Counting Kit-8(CCK-8) (Dojindo Inc., Kumamoto, Japan, CK04). CCK-8 treated cells were incubated for 1 h. Then, the absorbance was measured at 450 nm with a SynergyMx fluorometer.

Immunostaining and morphological observation of cell

HGFs were seeded on each experimental substrate and cultured at 37 °C in the presence of serum. Cells were washed with PBS and fixed in 4% PFA in PBS for 10 min. After fixation, cells were washed with PBS and then treated with 0.1% Triton X-100 in PBS for 5 min and blocking solution (1% BSA in PBS) for 30 min. To visualize focal adhesions, cells were treated with anti-vinculin antibody (Sigma, St. Louis, MO) diluted 1:400 in blocking solution for 1 h, followed by incubation with goat anti-mouse Alexa Fluor 488 antibody (Molecular Probes, Eugene,OR) at 1:400 dilution in blocking buffer for 1 h. For double labeling, TRITC-conjugated phalloidin was incubated simultaneously with the secondary antibody. Slides were washed three times with PBS between each antibody treatment. Images of cells on the substrates were collected using inverted fluorescence microscope (IX71, Olympus, Japan), and were analyzed by Metamorph software (Molecular Devices,

Sunnyvale, USA).

Gene expression analysis

For the investigation of mRNA expression change in the collected samples, mRNA was isolated from each cell-based sample treated with TRIzol (Invitrogen, USA, 15596018) and quantified by Synergy MX Multi-mode micro plate reader (BioTek, USA). Using 0.1–1 μg of total RNA, cDNA was synthesized by 5xRT-Master Mix with random hexamer (Elpisbiotech, Korea, EBT-1511) according to the instruction manual (reaction in a 20 μL volume at 42ºC for 60 min). For target gene amplification, each primer was referred from PrimerBank. Primer sequences were confirmed in Table 3.4.1. Real-time PCR was conducted to quantify mRNA. Each reaction was conducted in a 20 μL volume with 10–100 ng of cDNA and 0.2 μM of each primer by using POWER SYBR green PCR master mix (Applied Biosystems Inc., USA, 4367659). CFX Connect Real-Time PCR System (Bio-Rad, USA) was utilized in this study in two-step amplification process (annealing/extension at 60ºC for 1 min and denaturation at 95ºC for 15 sec) with melting curve analysis. The result data were analyzed by a CFX Maestro 1.0 software (Bio-Rad, USA). Threshold cycle (Ct) was automatically determined. Since NTC group showed Ct value over 38, we disposed of the result data over 38 Ct. GAPDH is used to normalize the gene expression data as an endogenous control in the quantitative analysis of RT-PCR.

Primer sequence information

Target	Forward primer	Reverse primer	Access-ion #	size (bp)
GAPDH	TCACTGCCACCCA GAAGACTG	GGATGACCTTGCC CACAGC	NM_002 046	123
ITGB1	GTAACCAACCGTA	TCCCCTGATCTTAA	NM_033	98

	GCAAAGGA	TCGCAAAAC	668	
FAK	GCTTACCTTGACC	ACGTTCCATACCA	NM_153	75
	CCAACTTG	GTACCCAG	831	
VCL	CTCGTCCGGGTTG	AGTAAGGGTCTGA	NM_003	95
	GAAAAGAG	CTGAAGCAT	373	
TAL	TACATGCTCCGAA	ACCATGATCGTCTT	NM_006	142
	ATGGGGAC	CACAGTTC	289	

Table 3.4.1 Primer sequences for the real-time PCR analysis

3.5 References

1. Guillaume, B., *Morphologie* **2016,** *100* (331), 189-198.
2. Duraccio, D.; Mussano, F.; Faga, M. G., *J Mater Sci* **2015,** *50* (14), 4779-4812.
3. Kim, M. H.; Park, K.; Choi, K. H.; Kim, S. H.; Kim, S. E.; Jeong, C. M.; Huh, J. B., *Int J Mol Sci* **2015,** *16* (5), 10324-36.
4. Sculean, A.; Gruber, R.; Bosshardt, D. D., *J Clin Periodontol* **2014,** *41 Suppl 15*, S6-22.
5. Zhao, B.; van der Mei, H. C.; Subbiahdoss, G.; de Vries, J.; Rustema-Abbing, M.; Kuijer, R.; Busscher, H. J.; Ren, Y., *Dent Mater* **2014,** *30* (7), 716-27.
6. Abdallah, M. N.; Badran, Z.; Ciobanu, O.; Hamdan, N.; Tamimi, F., *Adv Healthc Mater* **2017,** *6* (20).
7. Atsuta, I.; Ayukawa, Y.; Kondo, R.; Oshiro, W.; Matsuura, Y.; Furuhashi, A.; Tsukiyama, Y.; Koyano, K., *J Prosthodont Res* **2016,** *60* (1), 3-11.
8. Nicholson, J. W., *Prosthesis* **2020,** *2* (2), 100-116.
9. Lee, J.; Kim, J.; Kim, S.; Min, D. H., *Adv Drug Deliv Rev* **2016,** *105* (Pt B), 275-287.
10. Kim, J.; Park, S. J.; Min, D. H., *Anal Chem* **2017,** *89* (1), 232-248.
11. Maleki, M.; Zarezadeh, R.; Nouri, M.; Sadigh, A. R.; Pouremamali, F.; Asemi, Z.; Kafil, H. S.; Alemi, F.; Yousefi, B., *Biomol Concepts* **2020,** *11* (1), 182-200.
12. Ryoo, S. R.; Kim, Y. K.; Kim, M. H.; Min, D. H., *ACS Nano* **2010,** *4* (11),

6587-98.

13. Hummers, W. S.; Offeman, R. E., *J Am Chem Soc* **1958,** *80* (6), 1339-1339.

14. Kumar, S.; Parekh, S. H *Commun Chem* **2020,** *3* (1).

15. Lee, W. C.; Lim, C. H.; Shi, H.; Tang, L. A.; Wang, Y.; Lim, C. T.; Loh, K. P., *ACS Nano* **2011,** *5* (9), 7334-41.

16. Ku, S. H.; Park, C. B., *Biomaterials* **2013,** *34* (8), 2017-23.

17. Elter, P.; Lange, R.; Beck, U., *Langmuir* **2011,** *27* (14), 8767-75.

Chapter 4. Conclusion

In summary, we have shown how nanobiotechnology can be used to solve problems in the life sciences. By using a nanomaterial, graphene oxide (GO), we demonstrated its applications in 1) development of the biosensor with high-fidelity and 2) improvement of implant material's bioactivity.

First, we produced a GO-based biosensor named RheGO that can analyze the activity of a viral enzyme processing RNA. Compared to a conventional method like molecular beacon assay, RheGO has several advantages including simplicity, cost-effectiveness, and high reliability due to just adding GO into the reaction batch. Furthermore, RheGO exhibited high potential as an antiviral drug screening platform because the viral enzyme inhibitor selected by RheGO displayed significant antiviral effects *in vitro* and *in vivo*. Second, we demonstrated that the bioactivity of implant material, pure titanium, can be increased by coating the bioactive material, GO, on its surface. Compared to finely controlling the thickness and roughness of the oxide film, the GO coating has the advantage of shortening the manufacturing time and lowering the processing cost due to a very simple surface treatment. Moreover, this surface treatment showed excellent bioactivity because of significantly increasing the adhesion and proliferation of human gingival fibroblasts in the titanium. In addition, we proved this result at the molecular biological level through gene expression analysis. Therefore, we might present the direction of the surface treatment method for implant materials based on biological principles rather than empirical experimental results.

Thus, the expected benefits from the research are as follows: 1) GO-based viral enzyme assay could be applied in the discovery of novel viral drugs to counter the

other viruses that may newly emerge in the future, and 2) regardless of the intrinsic properties of materials, various materials coated with GO might have the potential to become the implantation materials, leading to novel approaches in tissue engineering, prosthetic implant, and dental implant.

Summary in Korean (국문 요약)

산화그래핀을 이용한 항바이러스 약물 스크리닝 플랫폼 및 생리활성 임플란트 소재 개발

문명과 과학기술이 발전하면서 질병을 치료하기 위한 약물의 발굴 방법과 조직공학 기술 또한 함께 발전하였다. 그러나 생명과학 분야에서 상대적으로 주목받지 못하여 아직도 해결되지 않은 문제들이 존재하고 있다. 대표적인 예로서 바이러스 감염 질환 치료제 발굴을 들 수 있다. 세계화된 현대 사회에서 바이러스 감염으로부터 인류를 보호하고 치료하는 것이 얼마나 중요한지는 이루 말할 수 없다. 그러나 바이러스의 다양성과 빠른 변이의 출현으로 인해 기존의 약물 개발과정으로는 신속한 대응이 불가능하다는 한계가 있다. 따라서 이를 극복하기 위한 새로운 약물 발굴방법 개발과 이를 이용한 신속한 항바이러스 약물 발굴을 해야 한다. 또 다른 예로서, 임플란트 물질의 생리활성을 높이는 것이다. 외부 물질을 생체 내로 삽입할 때 생체내 부정적인 영향이 나타나지 않도록 하는 생체 적합도는 필수적이지만, 인공삽입술에서 인공삽입물질과 생체분자및 세포들 간의 강력한 상호작용을 할 수 있도록 생리활성을 높이는 것은 인공삽입물질의 장기간 안정성을 확보할 수 있다는 점에서 더욱 중요한 의미를 갖는다. 비록 인공삽입물로 활용될 수 있는 물질 종류가 다양하지 않지만, 그럼에도 불구하고 물질의 표면 특성을 여러가지 방법으로 조절하여 생리활성을 높이는 연구들이 수행되고 있다. 그러나 물질 표면의 산화막

두께 및 거칠기를 조절하는 섬세한 방법에 비해 다소 간편한 개질 방법에 대한 요구가 지속되고 있다.

나노바이오기술은 원자나 분자 단위에서의 물성을 규명하여 새로운 물질을 개발하는 나노기술과 이를 이용하여 인간의 질병 및 생명현상을 연구하는 바이오기술이 결합된 것으로서, 고전적인 접근 방법으로 해결하지 못한 생물학 및 생명공학적 문제를 해결할 수 있는 기술이다. 그렇기 때문에 새로운 나노물질을 개발하고 뛰어난 물성을 갖는 나노물질을 바이오센서, 바이오칩, 약물전달, 치료제, 조직재생과 같은 다양한 분야에 적용시키는 것이 나노바이오기술의 핵심이라 할 수 있다.

특히, 다양한 나노물질 중에서 산화그래핀은 산소 작용기와 그래핀 도메인을 가지고 있으며 이로 인해 뛰어난 물리화학적 특징을 보이는 매력적인 나노물질이다. 대표적인 특징으로서, 산화그래핀은 표면에 흡착되거나 20 nm 내에 위치한 형광물질을 소광 시킬 수 있다. 이를 기반으로 다양한 형광 기반 바이오센서연구에 산화그래핀이 활용되고 있다. 또한 산화그래핀은 뛰어난 생체적합성과 뼈 재생 및 세포 분화를 유도할 수 있는 생리활성 특징을 가지고 있다. 이와 같은 특징으로 인해, 재생의학 및 인공삽입물 연구에 산화그래핀이 쓰이고 있다.

본 논문에서 우리는 산화그래핀을 이용하여 앞서 언급한 두 가지 문제에 대한 해결방법을 제시하고자 한다. 첫째, 신속한 항바이러스 약물 발굴을 위한 약물 스크리닝 플랫폼 기술 개발: 우리는 산화그래핀 기반의 RNA 바이러스성 헬리케이즈 활성 분석 기술인 RheGO를 개발하였다. 형광이 개질된 핵산 기질을 사용하여 실시간으로

핼리케이즈의 활성을 확인할 수 있는 본 분석 기술은 뛰어난 재현성과 신뢰성을 보여주었고, 항바이러스 약물 스크리닝에 적용이 가능함을 보였다. 그리고 발굴된 약물 후보군의 세포 수준 및 동물모델 수준에서 유의미한 항바이러스 효과를 확인하였다. 둘째, 임플란트 물질의 생리활성도 향상: 우리는 산화그래핀을 임플란트 물질 표면에 부착하여 그 영향을 확인하였다. 연구 결과 우리는 임플란트 물질에 산화그래핀을 코팅하면 치은섬유아세포의 부착 및 증식이 증가함을 확인하였다. 그리고 이는 치은섬유아세포가 산화그래핀과 접촉할 때 초점접착 유전자의 발현이 증가되어 나타난 결과임을 확인하였다.

본 연구 결과에서 우리는 고전적인 방법으로 해결하기 어려운 문제를 나노바이오기술을 이용한 새로운 접근법으로 해결할 수 있음을 보여주었다. 따라서 우리는 나노 물질인 산화그래핀을 활용하여 항바이러스 약물 발굴을 위한 새로운 방법 개발 및 조직공학을 위한 생리활성이 뛰어난 새로운 물질을 개발함으로써, 향후 많은 의료 및 생명공학 문제들을 해결할 수 있을 것으로 기대한다

주 요 어: 나노바이오기술, 산화그래핀, 바이오센서, 고효율 분석법, 항바이러스 약물 발굴, 생리활성 재료, 임플란트

학 번: 2014 - 21257

Acknowledgement

길었던 학위 과정을 마무리 짓게 되었습니다. 돌아보면 다사다난했던 학위 과정이었던 것 같습니다. 그런데도 많은 동료 연구자들 또한 같은 길을 걸어왔을 것을 생각해본다면 또한 많은 사람의 도움으로 학위 과정을 마칠 수 있었기 때문에 겸손함과 감사의 마음을 가질 수밖에 없는 것 같습니다.

학위 과정을 무사히 마칠 수 있게 해주신 지도교수님이신 민달희 교수님께 감사하다는 말씀을 드리며, 학위논문 심사에 참여해주셔서 아낌없는 조언을 해주신 홍종인 교수님, 홍병희 교수님, 이연 교수님, 장홍제 교수님께 다시 한번 감사의 말씀을 드리고 싶습니다. 또한 공동 연구를 수행한 전북대학교의 장용석 교수님과 박지상 박사님, 고려대 우재성 교수님, 서울대 치의학과 여인성 교수님과 곽정민 연구원님께 감사의 말씀을 드리고 싶습니다. 그리고 함께 고생한 연구실 동료들인 성민, 예지, 세열, 호정, 수민에게는 감사의 말과 조금 더 힘내라는 응원을 보내고 싶습니다. 비록 입학 연차는 다르지만 가장 많은 논의와 고민을 함께 공유하였던 안민철 박사, 송재광 박사에게도 감사의 말을 전하고 싶습니다. 학위 과정 동안 많은 힘이 되어준 고등학교 및 대학교 친구들 및 11화학대대 전우들께 감사합니다. 그리고 먼저 학위를 받은 선배로서 저를 지지해주시고 응원해주신 아버지께 감사드리며 저의 깊은 고민을 들어주시고 위로와 격려를 해주신 어머님께 감사드립니다. 또한 가족 친지분들과 귀여운 조카 소유, 온유, 유하, 선하 덕분에 많은 힘을 얻을 수 있었던 것 같습니다. 그리고 저에게 늘 테크니션이 아닌

생각하는 과학자가 되라는 아낌없는 조언을 주셨던 학부 지도교수님이신 김상희 명예교수님께 감사드립니다. 마지막으로 연구를 수행하면서 많은 도움과 함께 고민해준 박세진 박사님께 진심어린 감사를 드립니다.

여러분들의 도움과 응원이 없었다면 학위 과정을 마치지 못하였을 것입니다. 다시 한번 감사합니다.

Curriculum Vitae

Jungho Kim

Department of Chemistry
Seoul National University
Gwanak-ro 1, Gwanak-gu,
Seoul 08826, Korea
E-mail: junghokim@snu.ac.kr
Tel: +82-10-4736-5019

EDUCATION

Mar.2014 – Feb.2022 **M.S / Ph.D. integrated course**,
Seoul National University, Seoul, Korea
Major: Nanobio Chemistry
Advisor: Prof. Dal-Hee Min

Mar.2007 – Feb.2014 **B.S.**
Konkuk University, Seoul, Korea
Major: Chemistry
Advisor: Prof. Sang Hee Kim

Thesis: *The pan-neural genes, deadpan and scratch, are required for proper formation, division and differentiation of neuroblasts in the Drosophila central nervous system*

PUBLICATIONS

Jungho Kim, Se-Jin Park, Jisang Park, Hojeong Shin, Yong-Suk Jang, Jae-Sung Woo, and Dal-Hee Min*, "Identification of a direct-acting antiviral agent targeting RNA helicase via a graphene oxide nanobiosensor", *ACS Applied Materials & Interfaces*, **2021**, *13*(22),25715-25726

Hojeong Shin, Se-Jin Park, **Jungho Kim**, Ji-Seon Lee and Dal-Hee Min*, "A graphene-based fluorescent nanosensor to identify antiviral agents via a drug repurposing screen", *Biosensors & Bioelectronics*, **2021**, *183*, 113208

Ji-Seon Lee, **Jungho Kim**, Hojeong Shin, and Dal-Hee Min*, "Graphene oxide-based molecular diagnostic biosensor for simultaneous detection of Zika and dengue viruses", *2D Materials,* **2020**, *7*, 044001

Se-Jin Park, **Jungho Kim**, Seoung-Hoon Kang, Hyung Jin Cha, Hojeong Shin, Jisang Park, Yong-Suk Jang, Jae-Sung Woo, Cheolhee Won, and Dal-Hee Min*, "Discovery of direct-acting antiviral agents with a graphene-based fluorescent nanosensor", *Science Advances*, **2020**, *6(22)*, eaaz8201

Seounghun Kang, Jun Kim, Minchul Ahn, **Jungho Kim**, Myeonggang Heo, Dal-Hee Min*, Cheolhee Won, "An RNAi nanotherapy for fibrosis: Highly durable knockdown of CTGF/CCN-2 by using siRNA-DegradaBALL (LEM-S401) to treat skin fibrotic diseases", *Nanoscale,* **2020**, *12*, 6385-6393

Hojeong Shin, Se-Jin Park, Yeajee Yim, **Jungho Kim**, Chulwon Choi, Cheolhee Won, and Dal-Hee Min*, "Recent advances in RNA therapeutics and RNA delivery systems based on nanoparticles", *Adv. Therap.* **2018**, *1(7)*, 1800065

Jungho Kim, Se-Jin Park, and Dal-Hee Min*, "Emerging approaches for graphene oxide biosensor", *Anal. Chem.*, **2017**, *89*, 232-248

Jieon Lee, **Jungho Kim**, Seongchan Kim, Dal-Hee Min*, "Biosensors based on graphene oxide and its biomedical application", *Adv. Drug Deliv. Rev.*, **2016**, *105*, 275-287

Hyeon Ju Kim, Hui Jeong Ahn, Sihaeng Lee, **Jung Ho Kim**, Jisun Park, Sang-Hak Jeon, Sang Hee Kim*, "Intrinsic dorsoventral patterning and extrinsic EGFR signaling genes control glial cell development in the *Drosophila* nervous system", *Neuroscience*, **2015**, *307*, 242-252

REFERENCES

Prof. Dal-Hee Min (M.S and Ph.D. Advisor)

Department of Chemistry, Seoul National University

Seoul 08826, Korea

Tel: +82-2-880-4338

E-Mail: dalheemin@snu.ac.kr